Quarterly Report for

Contract DE-FG36-08GO18192

Stanford Geothermal Program

October-December 2009

Table of Contents

1. FRACTURE CHARACTERIZATION USING PRODUCTION DATA

This research project is being conducted by Research Assistant Egill Juliusson, Senior Research Engineer Kewen Li and Professor Roland Horne. The objective of this project is to investigate ways to characterize fractures in geothermal reservoirs using production data.

1.1 SUMMARY

This report discusses a simulation study of tracer and thermal transport in fractured geothermal reservoirs. The motivation was to explore the relationship between tracer returns and thermal breakthrough in fractured geothermal reservoirs. Moreover, we wanted to explore in more detail the possibility of simulating combined tracer (mass) and thermal transport where individual fractures are modeled explicitly.

By employing the fracture discretization method introduced by Karimi-Fard et al. (2003), we were able to run simulations with fracture grid blocks of realistic dimension. This enabled us to obtain relatively realistic models of tracer and thermal transport and investigate the sensitivity of the return profiles to various reservoir properties. Additionally, the visualization of changes in temperature, pressure and tracer concentration in the reservoir were useful to for gaining deeper insight into the behavior of these properties in the fractured systems.

The initial plan was to use the TOUGH2 code to do the simulations, but after running into a number of problems with the solver and time stepping it was decided to switch to the General Purpose Research Simulator (GPRS) developed at the Department of Energy Resources Engineering at Stanford University. The simulations were carried out using a two-dimensional thermal black-oil model, without gravity effects.

In short we found that a quantitative relationship between the tracer return profile and the thermal return profile is hard to formulate explicitly, even for relatively simple cases. The relationship will depend, for example, the flow rate through the fracture and the types of boundary conditions for the matrix surrounding the fracture. Moreover, the fracture distribution will be important, although in the case investigated here, the thermal profile was not as severely affected as anticipated.

1.2 INTRODUCTION

The motivation for this work was, in part, to investigate the extent to which tracer returns could be used to predict thermal breakthrough in fractured reservoirs. The topic has previously been discussed e.g. by Bodvarsson and Pruess (1984), Urbino and Horne (1991), Sullera and Horne (2001), Horne and Szucs (2007) and Juliusson and Horne (2009b). This idea becomes particularly interesting with regards to optimization of reinjection scheduling, as discussed by Lovekin and Horne (1989). However, the tracer testing approach has some limitations since the returns from a tracer test will vary with changes in the reinjection schedule. Moreover, Pruess and Bodvarsson (1984) showed that in vertically fractured reservoirs the tracer signal will not suffice to fully characterize the thermal characteristics of the flow path. They state that the flow path characteristics can be determined more accurately using a mixed numerical/semianalytical approach with the

combined interpretation of pressure, temperature and tracer. These analyses show that understanding the combined transport of pressure, tracer and heat in fractured reservoirs is an essential but non-trivial task.

Simulation of tracer transport in fractured reservoirs is also a particularly challenging problem. One reason is that for the most commonly used discretization schemes the computations will be adversely affected if a saturation front is allowed to travel more than one gridblock per time step. This obviously causes problems in models with saturations travelling fast through extremely small gridblocks. Lately some intriguing advances have been made to (partially) solve this problem. An efficient simulation technique for tracer transport in fractured reservoirs, using a discrete fracture discretization was illustrated by Lange et al. (2005), where a double-upstream discretization scheme was used to minimize numerical diffusion in a mass transport model. Wu and Forsyth (2008) added similar advancements (a flux-limiter scheme) for tracer dispersion to the TOUGH2 simulation code (which simulates mass and thermal transport). This particular update of the code is however not yet available to the public. With the approach of Wu et al. (2000, 2008) the explicit modeling of the fracture gridblocks is avoided by assigning a full tensor dispersion coefficient to relatively large gridblocks.

Combined simulation of tracer and thermal transport in explicitly modeled fractures has, to our knowledge, only been carried out using; a) simple Cartesian grids or; b) with two-dimensional models where the heat exchange with the fracture walls is approximated with a semi-analytical model for the cooling of the fracture walls, using the formulation of Vinsome and Westerveld (1980).

In this work we have utilized the method of Karimi-Fard et al. (2003) to discretize the permeability on an unstructured two-dimensional grid. This way the transport physics in the fracture network are captured more accurately, especially in sparsely fractured rock such as might be encountered in Enhanced Geothermal Systems (EGS). This simulation method is also interesting since it allows clear visualization of the propagation of the simulated properties (pressure, temperature, tracer saturation etc.) in time. However, with more densely fractured rock, this method quickly becomes infeasible because of the lack in computational efficiency. In such cases, an upscaling method could provide a practical alternative (e.g. Gong, 2007).

1.3 DISCRETE FRACTURE MODEL

This section describes briefly how the reservoir simulations were set up to simulate flow through fractured medium.

The first step in setting up the model was to generate a fracture network. A number of software packages are available for creating these, e.g. FRACMAN from Golder and Associates and FRACA from Beicip-Franlab. However, in order to keep the study simple, a two-dimensional network was created in MATLAB with a code loosely based on the geomechanical process of fracture formation. Further discussion on the code can be found in Juliusson and Horne (2009).

After the fracture network had been generated, a suitable computational grid had to be formed. This was accomplished using the open source mesh generator Triangle (Shewchuk, 1996). The program and all associated commands and files are well described on the Triangle website, http://www.cs.cmu.edu/~quake/triangle.html. Figure 1.1 shows a stochastic fracture network with a conforming triangular grid.

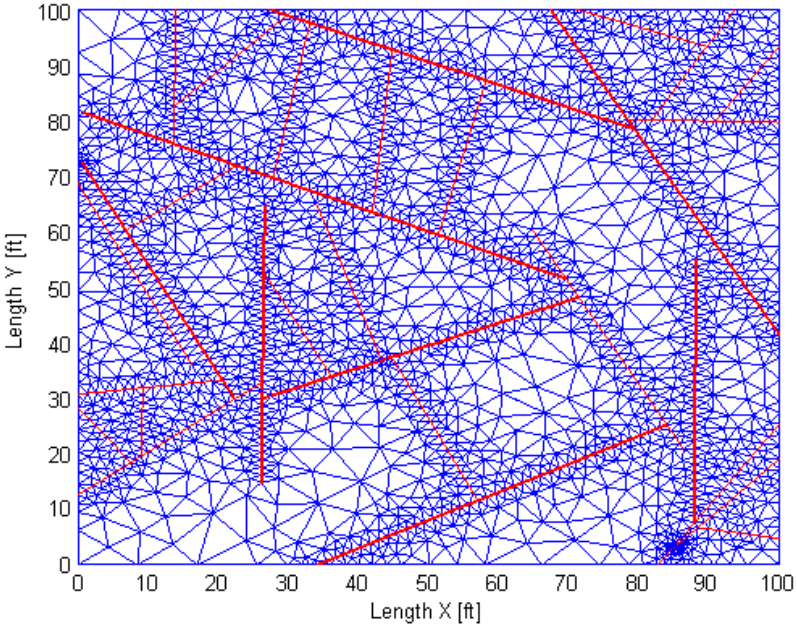

Figure 1.1: An example of a synthetic fracture network (red) and a mesh (blue) that conforms to the fractures. The width of the red lines is indicative of the width assigned to the fracture elements.

One of the major issues involved in modeling fractures explicitly in reservoir simulators relates to the intersection of the fractures. Handling this intersection in the "usual" manner leads to very small gridblocks (Figure 1.2) which can adversely affect the numerical stability and computational efficiency of the simulation.

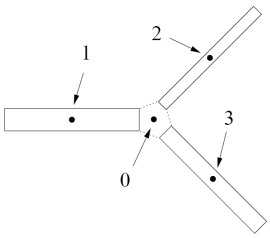

Figure 1.2: A very small gridblock (labeled 0) is formed at the intersection of fractures, on a computational grid where fractures are modeled discretely. Figure taken from Karimi-Fard et al. (2003).

By using the discretization scheme introduced by Karimi-Fard et al. (2003) the small gridblocks formed at fracture intersections were eliminated. The key element in their approach was to apply the star-delta transformation, which is more commonly used to solve problems in electrical engineering (Figure 1.3).

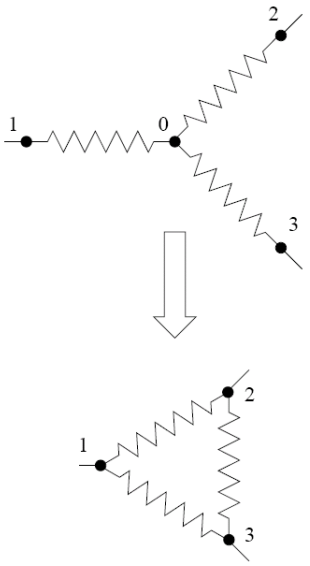

Figure 1.3: Intersections of multiple fractures can be converted to simpler connections using the star-delta transformation. Figure taken from Karimi-Fard et al. (2003).

From the star-delta transformation transmissibility between each connecting fracture element could be computed, using the formulation

$$T_{ij} = \frac{\alpha_i \alpha_j}{\sum_{k=1}^{n} \alpha_k} \tag{2.1}$$

where

$$\alpha_i = \frac{A_i k_i}{D_i} \tag{2.2}$$

and k denotes permeability, A is the cross sectional area at the fracture intersection and D is the distance from the centroid of the fracture block to the center of the fracture intersection.

Each fracture was assigned a width, w, and the corresponding permeability was determined by

$$k = \frac{w^2}{24} \tag{2.3}$$

For single-phase flow, the transmissibility values are related to the flow between two adjoining elements, *i* and *j*, by

$$Q_{ij} = \frac{T_{ij}}{\mu_{ij}}(p_j - p_i) \tag{2.4}$$

where Q is the flow rate, T is the transmissibility, μ is dynamic viscosity and p is the pressure in the corresponding gridblock.

Our initial plan was to use the TOUGH2 code to carry out the required simulation work. However, TOUGH2 was not equipped to handle transmissibility terms as input data for individual connections. To account for that, the TOUGH2 code was modified such that it could take permeability values as input through the connection list (CONNE). To be exact, the last column of the connection list (which is meant to contain data for radiative heat transfer, SIGX) was used as the input column for connection-wise permeability values. These permeability values were calculated using the transmissibility formulation given by equation (1), and then dividing by a similar number but calculated with $k = 1$, i.e.

$$k_{ij} = \frac{\alpha_i \alpha_j}{\sum_{k=1}^{n} \alpha_k} \Bigg/ \frac{\beta_i \beta_j}{\sum_{k=1}^{n} \beta_k} \tag{2.5}$$

where

$$\beta_i = \frac{A_i}{D_i} \tag{2.6}$$

Then the values D and A could be supplied in the usual way through the connection list and the transmissibility was recalculated internally in TOUGH2. Note that the permeability values supplied in the ROCKS section and/or ELEME section of the TOUGH2 input file were all set to one, such that they would not interfere with the values supplied through the connection list (CONNE).

The modified version of TOUGH2 seemed to work well, in the sense that it yielded physically realistic output for the tracer returns. However, we ran into trouble when running the code for longer simulation times which would be required to observe thermal breakthrough times. We believe that the problem is related to the time stepping algorithm and/or simply the fact that the set of equations involved are too hard to solve for the solvers used by TOUGH2.

As an alternative we decided to use the Stanford General Purpose Reservoir Simulator (GPRS) (Cao, 2002; Voskov, 2006). All simulations with GPRS were run using the black-oil thermal module, where water was injected into a fully "oil" saturated reservoir, where the "oil" phase had all the equivalent properties of water. Capillary pressure was set to zero and X-curve relative permeability was used such that the two phases would interact as if

there was only one phase. The pressure and temperature were set such that the reservoir fluid always remained as single phase liquid.

1.4 GOVERNING EQUATIONS

Before looking into simulations of specific fracture formations it was useful to review the governing equations of mass and energy rates for a unit volume, and see how much could be understood from employing some simplifying assumptions.

For single phase flow of κ components the mass equation can be written as (see notation in Table 1.1)

$$\frac{\partial}{\partial t}(\varphi\rho^{\kappa}X^{\kappa}) = -\nabla\left(\frac{k\rho^{\kappa}\nabla p}{\mu^{\kappa}}X^{\kappa} + \varphi\rho^{\kappa}d_{mol}^{\kappa}\nabla X^{\kappa}\right) + q^{\kappa} \tag{2.7}$$

The energy equation can be formulated as

$$\frac{\partial}{\partial t}\left(\varphi\rho^{\kappa}X^{\kappa}u^{\kappa} + (1-\varphi)\rho_{R}u_{R}\right) = -\nabla\left(\frac{k\rho^{\kappa}\nabla p}{\mu^{\kappa}}X^{\kappa}h^{\kappa} + \lambda\nabla T\right) + w^{\kappa} \tag{2.8}$$

Table 1.1: Notation used for governing equations.

φ	Porosity
ρ	Density (kg/m3)
X	Mass fraction of component
κ	Superscript that denotes component (water or tracer)
t	Time (sec)
k	Absolute permeability (m2)
p	Pressure (Pa)
μ	Dynamic viscosity (Pa-s)
d	Molecular diffusion coefficient (m2/s)
q	Mass source/sink (kg/s-m3)
u	Specific internal energy (J/kg)
R	Subscript that denotes rock
T	Temperature (C)

h	Specific enthalpy (J/kg)
λ	Thermal conductivity (W/m-C)
w	Energy source/sink (W/m3)
y	Distance (m)
c	Specific heat capacity (J/kg-C)
V	Subscript referring to volume

In most of the cases we considered the matrix permeability was much smaller than that of the fracture, and therefore the derivative along the fracture (here y direction) would dominate. Given that molecular diffusion is on the order of 10^{-10} for liquid tracers, we assumed that this could be discarded. For the temperature/pressure range observed, the density changes could be considered negligible over incremental distances in time and space. Therefore the mass balance equation could practically be reduced to

$$\varphi \frac{\partial}{\partial t}(X^\kappa) = -\frac{d}{dy}\left(\frac{kX^\kappa}{\mu^\kappa}\frac{dp}{dy}\right) + \frac{q^\kappa}{\rho^\kappa} \tag{2.9}$$

To further simplify the energy equation, the enthalpy and internal energy were written in terms of specific heat capacities, and these were assumed not to change much incrementally. This gave

$$\varphi \frac{\partial}{\partial t}\left(X^\kappa T + \frac{(1-\varphi)\rho_R c_R}{\varphi \rho^\kappa c_V^\kappa} T\right) = -\frac{d}{dy}\left(\frac{kX^\kappa c_p^\kappa T}{\mu^\kappa c_V^\kappa}\frac{dp}{dy}\right) - \frac{\lambda}{\rho^\kappa c_V^\kappa}\nabla^2 T + \frac{w^\kappa}{\rho^\kappa} \tag{2.10}$$

The thermal diffusion coefficient, $\lambda / c_V^\kappa \rho^\kappa$, was on the order of 10^{-3} m^2/s. Also the quantity

$$v = -\frac{k}{\mu}\frac{dp}{dy} \tag{2.11}$$

is the Darcy velocity. In many of the single fracture studies this velocity remained approximately constant (at around 10^{-3} m/s). Therefore Equations (2.9) and (2.10) would further simplify to

$$\varphi \frac{\partial}{\partial t}(X^\kappa) = v\frac{d}{dy}\left(X^\kappa\right) + \frac{q^\kappa}{\rho^\kappa} \tag{2.12}$$

and

$$\varphi \frac{\partial}{\partial t}\left(X^{\kappa}T + \frac{(1-\varphi)\rho_R c_R}{\varphi \rho^{\kappa} c_V^{\kappa}} T \right) = -v \frac{d}{dy}\left(\frac{c_p^{\kappa}}{c_V^{\kappa}} X^{\kappa} T \right) - \frac{\lambda}{\rho^{\kappa} c_V^{\kappa}} \nabla^2 T + \frac{w^{\kappa}}{\rho^{\kappa}} \tag{2.13}$$

The flow velocity was generally on the order of 10^{-3} m/s and the ratio of specific heat capacities was close to one.

Some further simplifications may be possible e.g. by placing the source/sink terms in the boundary conditions but in any case, this coupled system of partial differential equations remains complex – i.e. and ideal candidate for solution via numerical simulation.

1.5 STUDY OF A SINGLE FRACTURE

The first study undertaken was that of a single fracture. For the base case the fracture had 1 mm aperture, and length and height equal to 1 m. Water with temperature 100 C was injected on one end of the fracture and produced on the other. The flow velocity was kept constant at 1 mm/sec and the reservoir had an initial temperature of 200 C. To limit numerical dispersion the computational grid was set up such that the fracture was broken into 100, equally long segments (Figure 1.4). The boundaries were modeled as closed to both mass and heat transfer, at a distance of 0.5 m from the fracture walls, and the matrix had zero permeability.

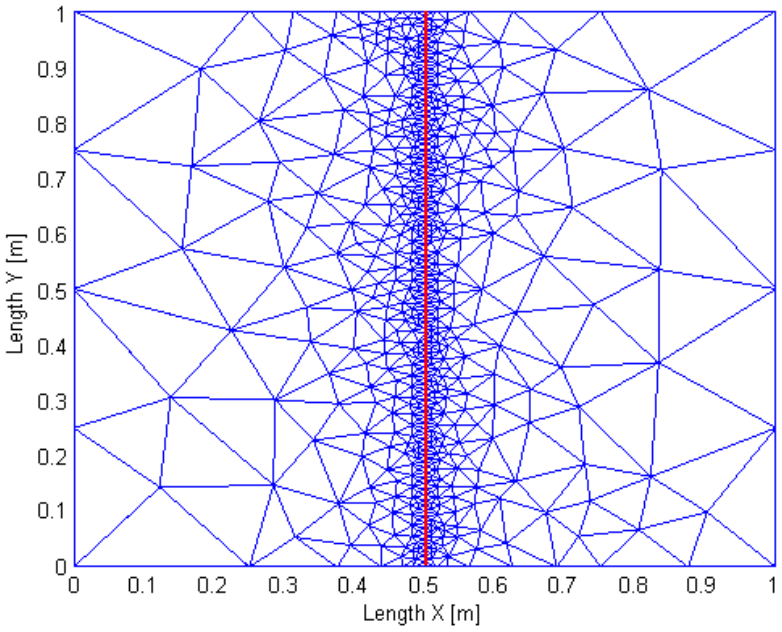

Figure 1.4: Computational grid for a single fracture, broken lengthwise into 100 segments.

The time step was limited to 200 seconds, for the first day of simulation. This way the estimated numerical dispersion (eq. (1.14), Lange, Bousian, and Bourbiaux, 2005) would be similar to the estimated Taylor dispersion (eq. (1.15), Horne and Rodriguez, 1983)

$$D_{num}^{imp.sat.} = \frac{v\Delta x}{2} + \frac{v^2 \Delta t}{2} \tag{2.14}$$

$$D_{Taylor} \approx \frac{2}{105} \frac{v^2 b^2}{d_{mol}} \tag{2.15}$$

Here v is flow velocity, and Δx and Δt are gridblock length and time step size, respectively, b is fracture aperture and d_{mol} is molecular diffusivity which is usually on the order of 10^{-10} m^2/s for tracers in liquid water. Note that the time step term in Eq. (2.14) dominates.

Figure 1.5 shows the normalized temperature and tracer returns on a logarithmic time scale.

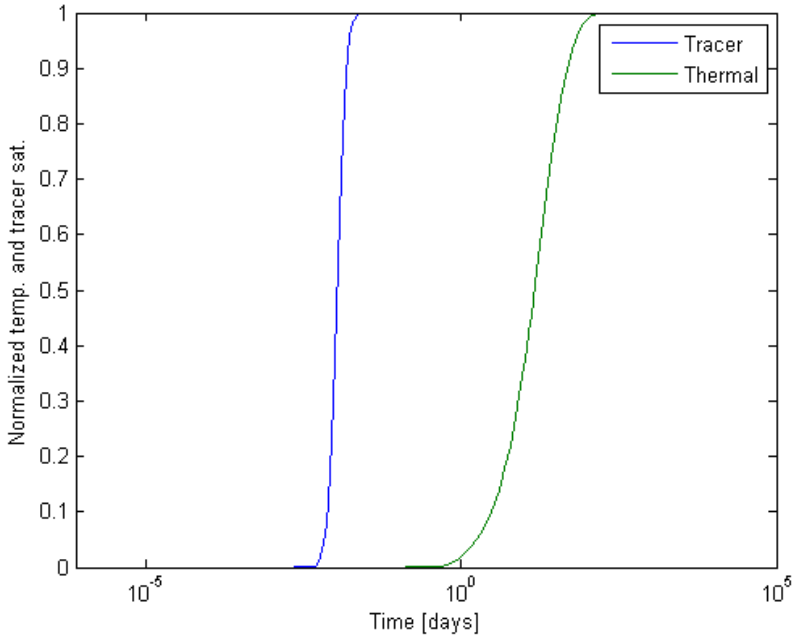

Figure 1.5: Normalized temperature and tracer returns for the base case.

The estimated arrival time was calculated as the point at which the return profiles reached the value 0.5. For the tracer this yielded $t_{tr,0.5} = \bar{t}_{tr} = 0.0107$ days, and for the temperature $t_{T,0.5} = \bar{t}_T = 14.6$ days.

The dispersion coefficient was calculated using the formulation (Bear, 1972)

$$D = \frac{1}{8}\left(\frac{t_{0.841} - t_{0.159}}{t_{0.5}} \right)^2 \frac{L^2}{t_{0.5}\varphi} \tag{2.16}$$

where L is the fracture length. In this case the tracer dispersion was $D_{tr} = 4.6 \times 10^{-5}\,\mathrm{m}^2/\mathrm{s}$ which was actually a bit less than predicted from Eq. (2.14) because the simulator automatically reduced the time step well below 200 sec during several of the first iterations. The dispersion coefficient for the temperature return was $D_T = 5.97 \times 10^{-7}\,\mathrm{m}^2/\mathrm{s}$.

Several variations of the base case were studied to gain understanding of the sensitivity of the return profiles to various factors

1.5.1 Varying Fracture Aperture

The first study undertaken was to vary the fracture aperture in the model. Note that the flow velocity was kept constant (as opposed to the injection rate). The aperture was given the values $b = \{0.1, 0.3, 1, 3, 10\}$ mm.

The tracer return profiles remained effectively the same for all cases, as expected since Taylor dispersion (eq. (2.15)) was not part of the simulation code. The thermal return curves however, varied considerably. In particular the mean thermal return times seemed to follow a trend where (see Figure 1.6)

$$\bar{t}_T \propto \frac{1}{b^n} \tag{2.17}$$

and n varied from approximately 1 for smaller apertures to around 2 as the aperture was made larger.

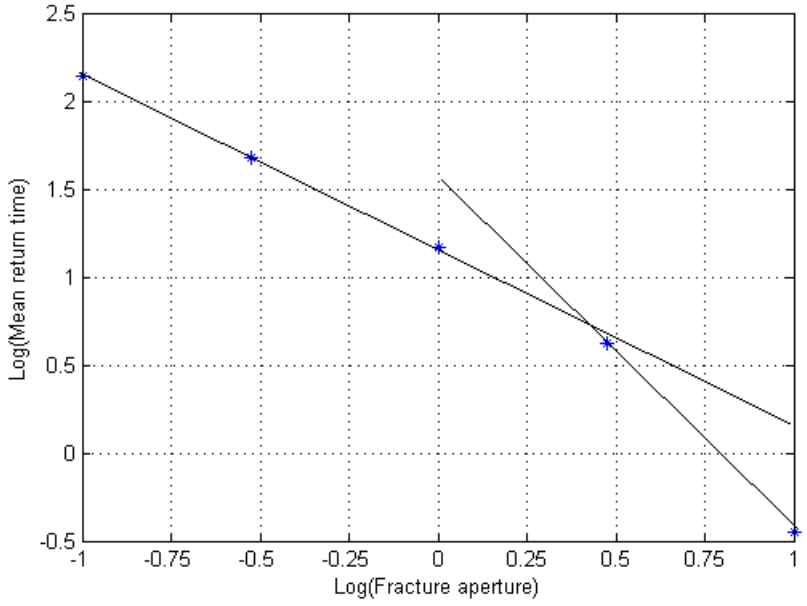

Figure 1.6: Logarithm of thermal front return time as a function of the logarithm of fracture aperture. The two illustrative lines have slope -1 and -2.

A similar trend was seen in the dispersion coefficient for the thermal return profile (Figure 1.7), i.e.

$$D_T = b^m \tag{2.18}$$

where *m* seems to vary from around 1 to 4 as the fracture aperture gets larger.

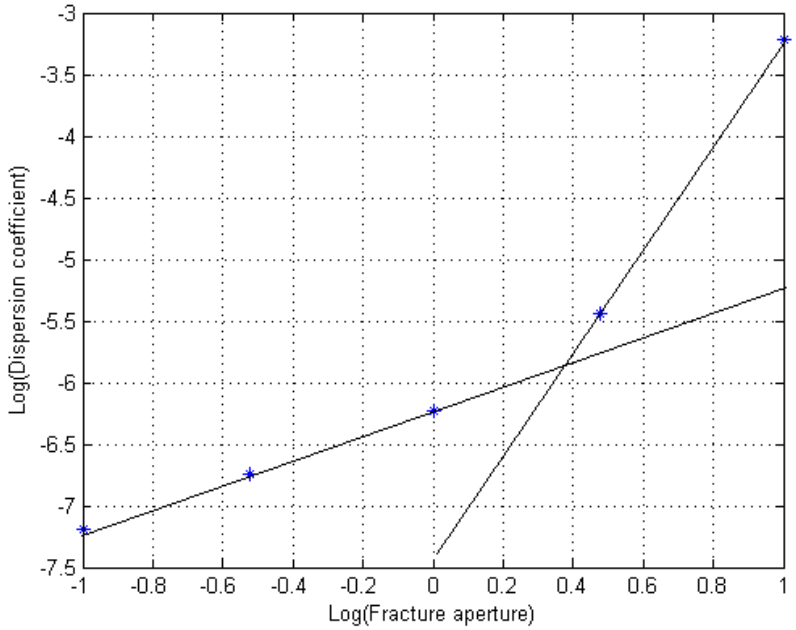

Figure 1.7: Logarithm of thermal front dispersion coefficient as a function of the logarithm of fracture aperture. The two illustrative lines have slope ~1 and ~4.2.

Although the models postulated here do not explain the variation in return times very accurately it is clear that both the thermal return time and dispersion are highly dependent on the fracture aperture. This is because flow velocity is kept constant and therefore the total flow rate through the fracture varies linearly with the aperture. This corresponds directly to the temperature decline for small apertures (flow rates) while for larger apertures (flow rates) the thermal decline becomes more rapid. The deviation from linearity is likely caused by interaction with the boundary although an explicit formulation for the boundary condition interaction was not found.

1.5.2 Varying Boundary Distance

The second parameter investigated was the distance from the fracture to the side boundaries, i.e. the length of the x-axis on Figure 1.4. The distance was varied from 0.25 to 50 m.

Again, the tracer front stayed more or less the same in all cases but the thermal front varied. As seen in Figure 1.8, the thermal return time varied approximately as the square

root of the boundary distance when the distance was small (0.25 to 2.5 meters). When the boundary distance got larger however, the thermal return time stopped increasing, because the size of the reservoir became "infinite acting", i.e. it was as if there was an open boundary.

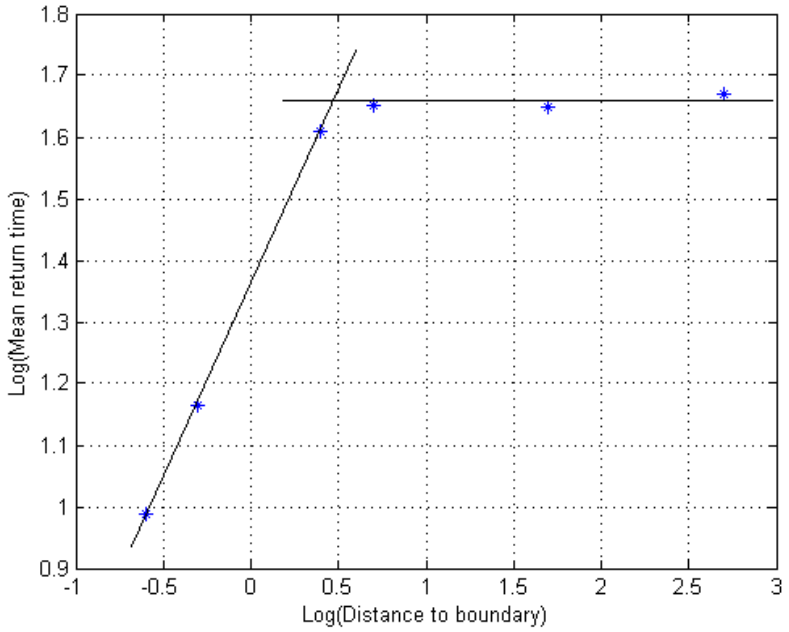

Figure 1.8: Logarithm of thermal front return time as a function of the logarithm of distance to the reservoir boundary. The two illustrative lines have slope ~0.5 and 0.

The thermal dispersion coefficient also ranged by a factor of about 10 in the various different cases, as can be seen in Figure 1.9. The trend in this case was not clear although one may propose that the three smallest distances are dominated by closed boundary effects, while the fourth is an intermediate case, and the two largest distances are representative of an open boundary.

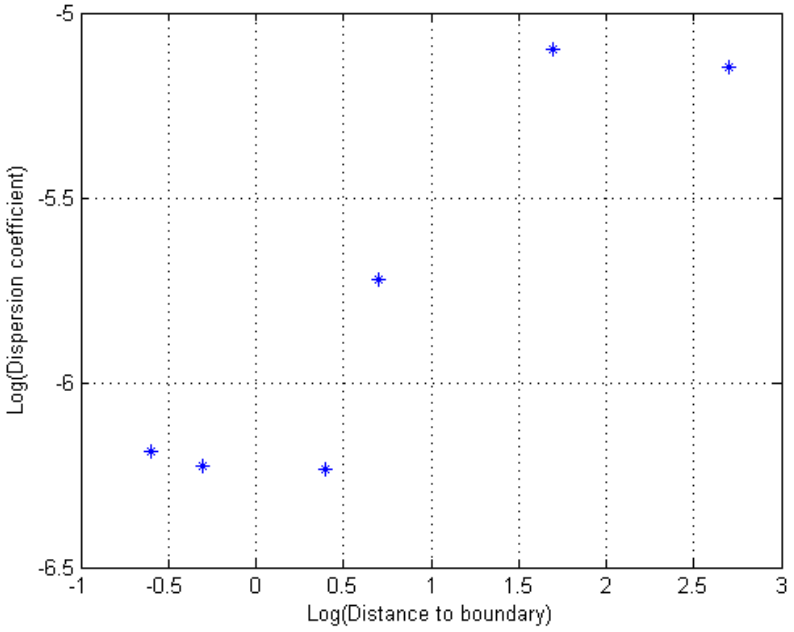

Figure 1.9: Logarithm of thermal front dispersion coefficient as a function of the logarithm of distance to the reservoir boundary.

1.5.3 Varying Flow Velocity

The effects of varying flow velocity were also studied. The flow velocity was varied in a similar way to the fracture aperture, i.e. $v = \{0.1, 0.3, 1, 3, 10\}$ mm/s. Here both the thermal and tracer return profiles varied from case to case. Of course the mean tracer return time was inversely proportional to the flow velocity. Moreover, the tracer dispersion coefficient increased with a close to linear relation to the flow velocity as seen in Figure 1.10.

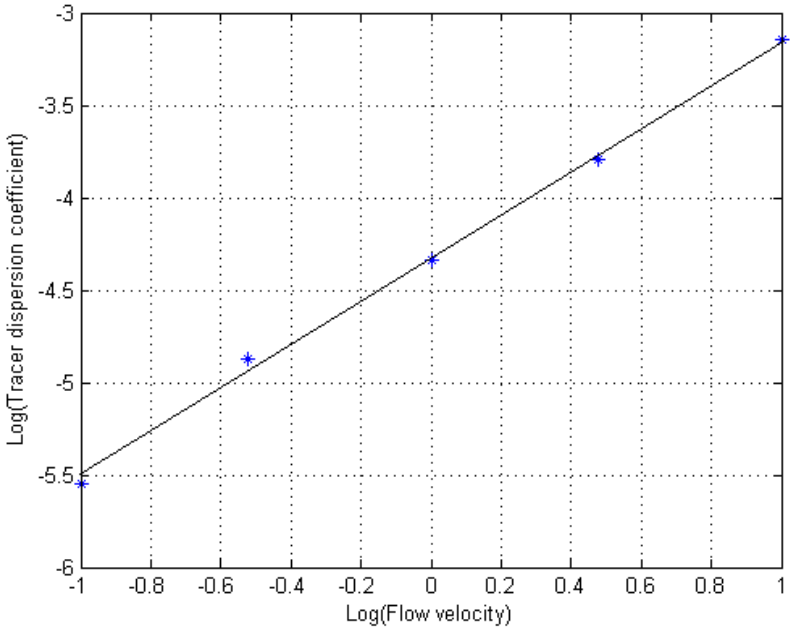

Figure 1.10: Logarithm of tracer front dispersion coefficient as a function of the logarithm of flow velocity. The illustrative line has slope ~1.2.

In fact the slope of the best line through the points in Figure 1.10 was around 1.2, that is

$$D_{tr} \propto v^{1.2} \tag{2.19}$$

which was not entirely in line with the expected value from Equation (2.14).The deviation could have been caused by the GPRS simulator automatically reducing the time step.
The thermal arrival time and dispersion coefficient behaved very similarly to the way they did in the varying aperture case as shown in Figure 1.11 and Figure 1.12.

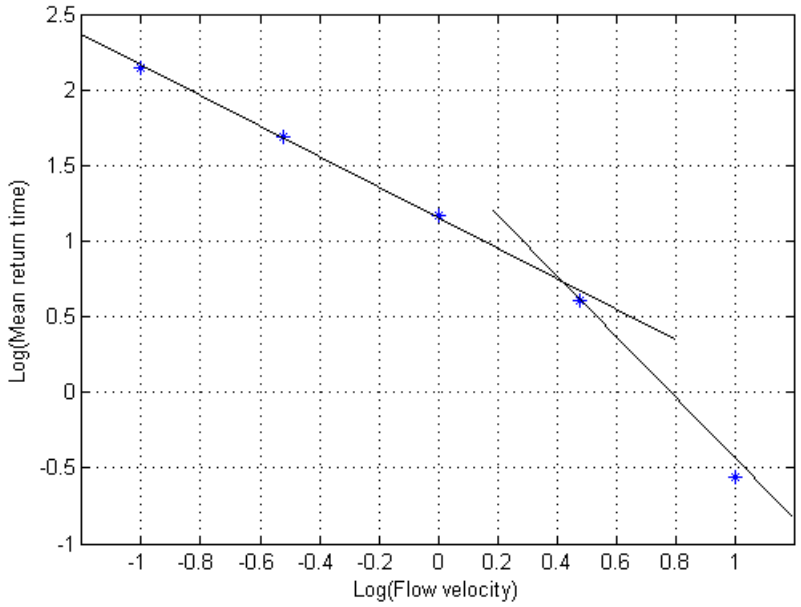

Figure 1.11: Logarithm of thermal front return time as a function of the logarithm of fracture flow velocity. The two illustrative lines have slope -1 and -2.

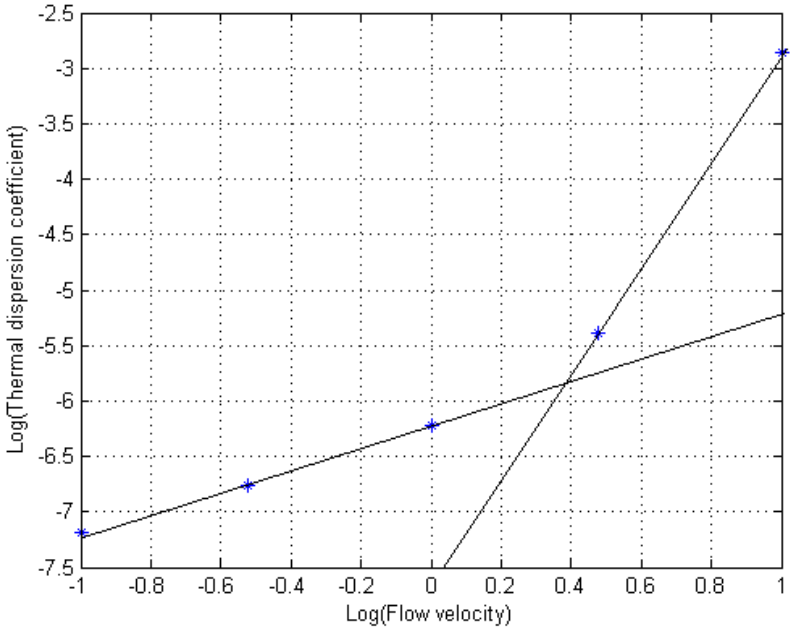

Figure 1.12: Logarithm of thermal front dispersion coefficient as a function of the logarithm of fracture flow velocity. The two illustrative lines have slope ~1 and ~4.6.

The reason for this similarity between the thermal behavior for the varying aperture and varying velocity case is that the total injection rate is the same in all corresponding cases.

Therefore, one might say that the thermal return profile is very sensitive to the flow rate through the fracture, rather than the velocity or the aperture. These three quantities are of course all related through Darcy's law

$$Q = bHv(b) = bH\frac{k(b)}{\mu}\frac{dp}{dy} = H\frac{b^3}{24\mu}\frac{dp}{dy} \tag{2.20}$$

Here Q is the volumetric flow rate H is the fracture height and all other quantities as defined earlier.

1.5.4 Other cases

A few other cases were studied in addition to those above. For example, varying the injection temperature had almost no effect on the return profiles. Increasing the matrix permeability up to 100 md also had very little effect.

Modeling an open boundary by giving the edge blocks (at 0.5 m lateral distance) a very large volume was also considered. This lead to very little changes in the tracer profile but the thermal return changed in the sense that the cold water never fully broke through; in stead it came to a balance temperature of around 120 C.

1.6 STUDY OF MULTIPLY FRACTURED RESERVOIR

Observations for a single fracture seemed to suggest that the thermal return curves were highly dependent on the flow rate through the fracture and the distance to the matrix boundary. The distance to the boundary can in a sense be understood as the fracture density. Therefore we ran two cases, one with a sparsely fractured reservoir and another where a large number of smaller fractures had been added. The aperture of the fractures varied in linear relation to the fracture lengths, such that they spanned a range of about 0.1 to 10 mm. The size of the reservoir was also set to 100×100×100 meters and the matrix was given permeability 1 md. The injection rate was fixed at 10 kg/s. The sparse and dense fracture networks (with around 40 and 300 fractures, respectively) are shown in Figure 1.13.

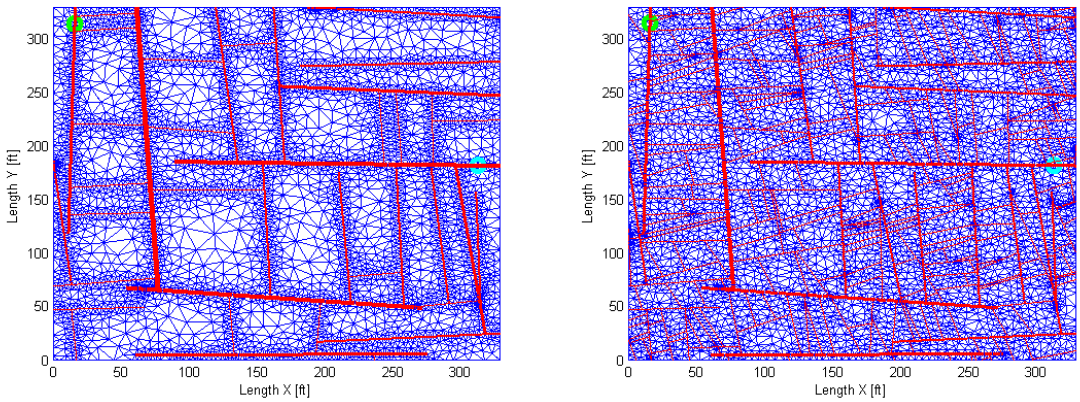

Figure 1.13: Sparse network of 40 fractures (above) and dense network of 300 fractures (below). The injector and producer are denoted by green and cyan circles, respectively. The width of the fracture lines (red) is indicative of the aperture.

1.6.1 Spatial Property Propagation

The propagation of pressure, temperature and tracer could be visualized and compared for the two cases. The following figures are snapshots of these property distributions after 12 hours of injection.

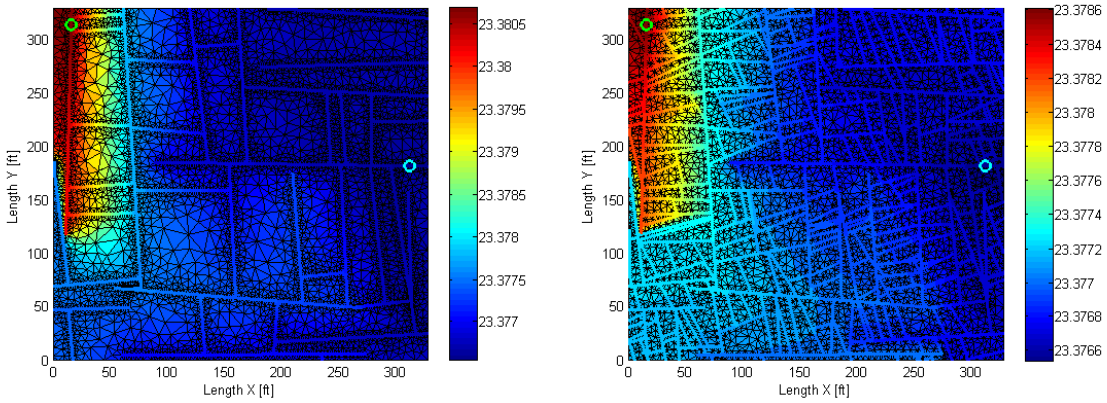

Figure 1.14: Pressure distribution after 12 hours of injection for the two fracture networks studied.

As Figure 1.14 shows, the pressure propagated in a diffusive nature as expected due to the elliptical character of the pressure equation. The pressure gradient spread considerably into the matrix in both cases, but in the denser network the pressure change spread further into the reservoir.

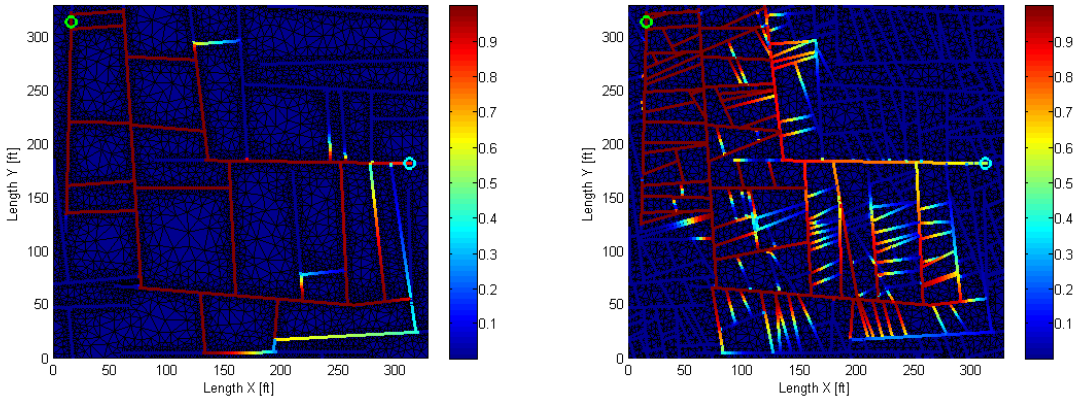

Figure 1.15: Tracer distribution after 12 hours of injection for the two fracture networks studied.

The tracer distribution in the reservoir is shown in Figure 1.15. The tracer propagation was dominated by convection (in fact diffusion effects were not modeled so the dispersion seen in the fractures is all numerical) and therefore the tracer flowed almost exclusively through the fractures. The flow through the denser network is clearly much more dispersive, which indicates that more effective heat extraction would be achievable.

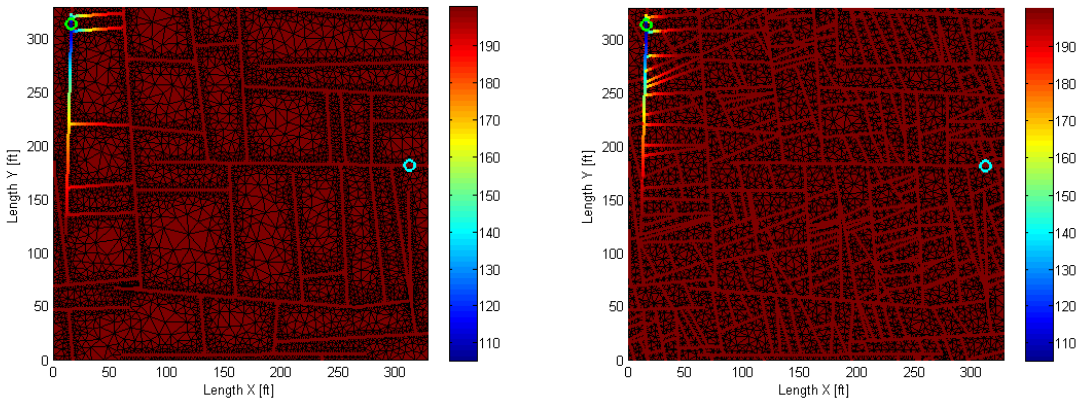

Figure 1.16: Thermal distribution after 12 hours of injection for the two fracture networks studied.

Figure 1.16 illustrates the temperature distribution after 12 hours of injection. At this time the thermal front seemed to be traveling mostly through the fractures. However, the front would not propagate much unless the surrounding matrix blocks had started cooling. This is perhaps better seen in Figure 1.17 which illustrates the thermal distribution after 280 days. Therefore one might say the thermal front traveled in a mixed convective/diffusive manner.

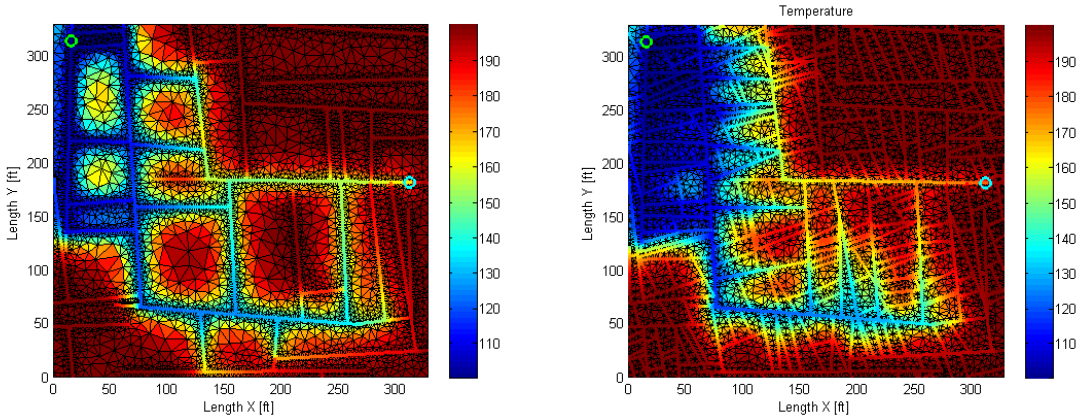

Figure 1.17: Thermal distribution after approx. 280 days of injection for the two fracture networks studied.

1.6.2 Return Profile Comparison

The main characteristics of the return profiles for the two simulation scenarios were computed in a manner similar to that for the single fracture cases. The results are summarized in Table 1.2.

Table 1.2: Characteristics of return profiles for the two simulation cases studied. Time is in days, dispersion is in m^2/sec

	$\overline{t}_{tr}$	D_{tr}	$\overline{t}_T$	D_T
Sparse	0.30	4.8×10^{-2}	425	3.1×10^{-4}
Dense	0.47	6.1×10^{-2}	546	1.0×10^{-4}

The denser network gave a longer mean return time for both the tracer and temperature. The change in the dispersion coefficient was however small, and for the temperature the dispersion coefficient was lower in the dense fracture network case. For the tracer this indicated that the density of the fracture network did not have as much effect on the dispersion coefficient as did numerical dispersion (or physically, Taylor dispersion, which would be similar in magnitude to the numerical dispersion). The fact that the thermal dispersion coefficient was smaller for the dense fracture network indicated that a more uniform front swept the reservoir.

The corresponding return curves from each of the simulation cases were compared on a quantile plot. This plot compares the times at which a certain quantile of the injection value is obtained on the production side. In Figure 1.18 the quantiles for the tracer return curves are compared. The fact that the quantile values all fell on the left of the 45 degree line meant that the tracer return time tended to be larger for the dense fracture case, and this difference got larger at later times.

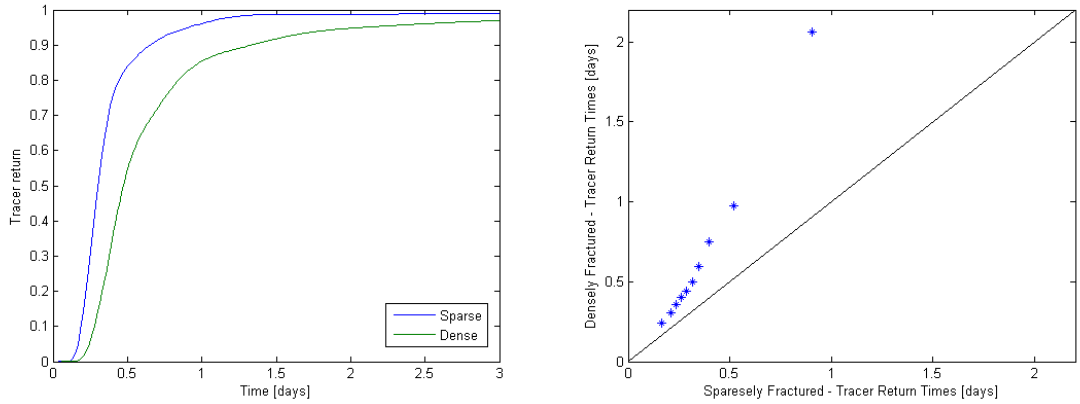

Figure 1.18: Comparison of the tracer return profiles for the sparse and dense fracture networks. The graph above is the derivative of the return profile. The graph below is a quantile plot comparing the two return distributions.

Figure 1.19 compares the two temperature return curves. These two return curves were clearly much more similar which was well conveyed on the quantile plot. For the dense fracture case the initial return quantiles were larger than those for the sparse case, but at later times the trend reversed. This pointed to a better thermal sweep in the dense fracture case. In other words, residual thermal energy was being swept from the reservoir for a slightly longer time in the sparse fracture case, and the bulk of the cooling came earlier.

As a final note of interest we mention that the tracer return profiles showed some "large scale" changes in the slope (Figure 1.18), which we believed to be strongly related to the fracture distribution. The thermal return showed more smooth variations (Figure 1.19) because of the strong thermal interaction with the matrix blocks.

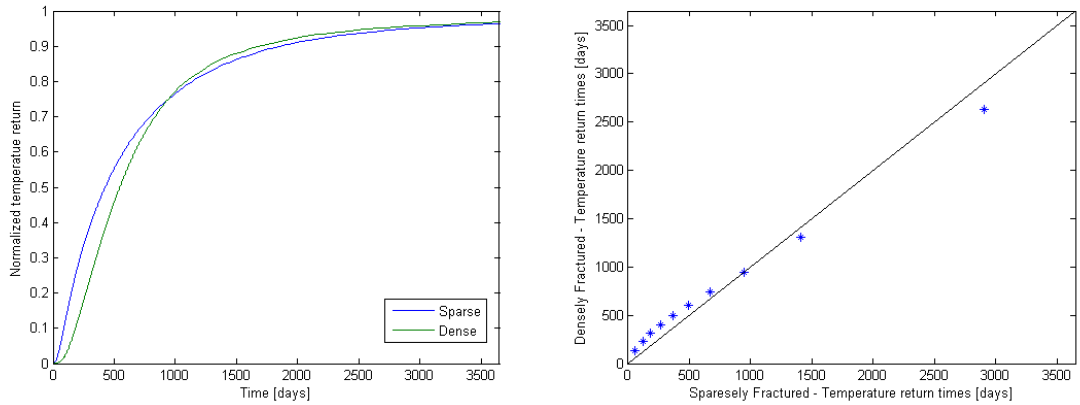

Figure 1.19: Comparison of the normalized temperature return profiles for the sparse and dense fracture networks. The graph above is the derivative of the return profile. The graph below is a quantile plot comparing the two return distributions.

1.7 FUTURE WORK

Some suggestions for future work of interest might be to try using an appropriate upscaling algorithm (e.g. Gong, 2007) and compare the results obtained to the method used here. This would be useful since the computational time for the dense fracture network was on the margin of being feasible. Another way to make these computations more efficient might be use a total variation diminishing scheme (Lange, Bousian, and Bourbiaux, 2005, Wu and Forsyth, 2008). Moreover, it seems like adding a formulation of Taylor dispersion should be possible if the explicit fracture discretization of Karimi-Fard et al. (2003) is used.

A more thorough analysis of the governing equations and the statistical relationship between fracture distributions and the return distributions would be of interest, although that seems to be a non-trivial task.

Finally the task of generating more realistic fracture network models should be addressed. This work would include an integrated analysis of various data sources ranging from conceptual geological models to seismic and resistivity measurement of the deep formations. An array of geostatistical methods are available for this type of analysis, although limited progress has been made with the characterization of fractured reservoirs.

1.8 CONCLUSIONS

The combined transport of tracer and temperature through a fracture network was studied through a number of simulations. The simulations were based on an efficient fracture discretization scheme developed by Karimi-Fard et al. (2003). The simulation code used was the General Purpose Research Simulator (GPRS) developed at the Department of Energy Resources Engineering at Stanford University.

The simulations on a single fracture showed that the thermal return profile is very sensitive to the extent of the matrix surrounding the fracture and the flow rate through the fracture.

Simulations on two fracture networks of varying fracture density indicated that the tracer return profile was more sensitive to the fracture density and/or connectivity, than was the thermal return profile. The thermal return profile did not vary as much since it was very much affected by bulk interaction with the matrix.

2. FRACTURE CHARACTERIZATION OF ENHANCED GEOTHERMAL SYSTEMS USING NANOPARTICLES

This research project is being conducted by Research Associates Mohammed Alaskar and Morgan Ames, Senior Research Engineer Kewen Li and Professor Roland Horne. The objective of this study is to develop in-situ multifunction nanosensors for the characterization of Enhanced Geothermal Systems (EGS).

2.1 SUMMARY

The slim tube experiment was initiated to test the feasibility of passing nanoparticles through longer pore networks than have previously been tested. Two 25 m sand-packed stainless steel tubes were constructed, as well as a 10 m sand-packed polypropylene tube. It was attempted to measure the gas permeability of the stainless steel tubes, but blockage within the tubes prevented this.

Four differential pressure transducers of different pressure ratings were calibrated for use in the slim tube experiment. Two of these transducers were also used in the gas and liquid permeability measurements of the polypropylene slim tube. An average gas permeability of 50 darcy and a liquid permeability of 49.9 darcy were observed. The tube was also determined to have a porosity of 35.5 % and a pore volume of 51.9 cm^3.

This report describes the motivation of the slim tube experiment, the construction of the slim tubes, the calibration of transducers, and the details involving the permeability and porosity measurements and calculations.

2.2 INTRODUCTION

Last quarter (July-September 2009), preliminary testing of different core samples and nanofluids continued, including the injection of SiO_2 nanoparticles into a Greywacke core. Greywacke sandstone is a very low permeability rock typical of geothermal reservoirs and therefore initial experimentation with it was indicative. An attempt to inject silver nanowires into a Berea sandstone core was also carried out, but the nanowires were not detected in the effluent. They were found to be trapped at the inlet section of the core within the pore network. In the current quarter, the design of sand-packed slim tubes was completed. In particular, two 25 m stainless steel sand packed slim tubes and a 10 m polypropylene sand packed slim tube were constructed. Standard measurements on the 10 m plastic tube were performed, including the gas and liquid permeability, porosity and pore volume measurements. The nanofluid injection experiment plan was also established.

2.3 MOTIVATION OF SLIM TUBE EXPERIMENT

The proof of concept of passing nanoparticles through porous media has been established for a short core but not over longer distances approaching those encountered in a subsurface reservoir. In order to investigate flow through a longer pore network, several slim tube apparatuses were designed and constructed. Initially, two 25 m stainless steel

tubes were made and packed with sand. Once packed, the tubes were wound in coils, and sampling valves were installed at intervals along its length. The objective in choosing stainless steel was so that the slim tube can be used in an air bath for high temperature experiments. One of these stainless steel slim tubes is pictured in Figure 2.1a.

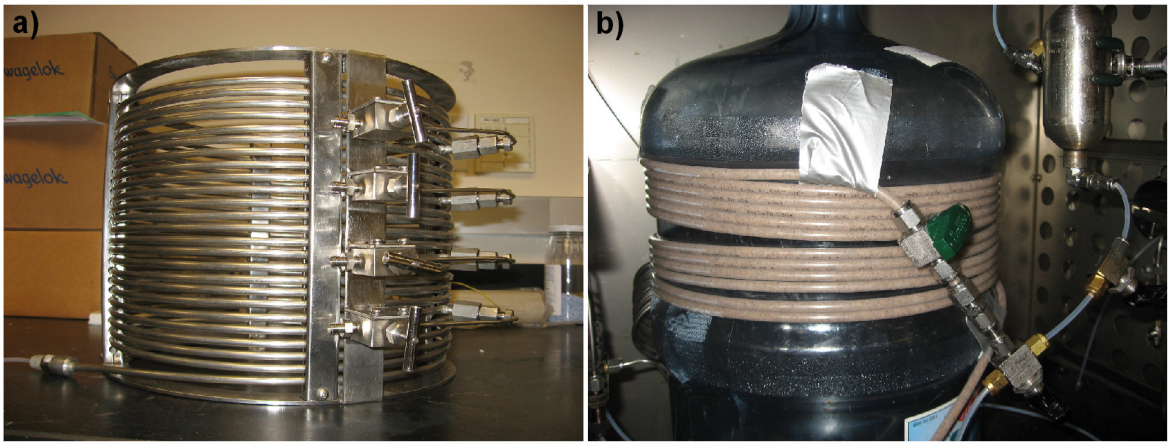

Figure 2.1: a) Stainless steel slim tube b) Polypropylene slim tube

A 10 m polypropylene slim tube apparatus was also constructed for more immediate use at room temperature. The tube was packed with sand of 1 mm maximum diameter and fitted with filter paper, screens, and valves at each end. This polypropylene slim tube is pictured in Figure 2.1b.

2.4 EXPERIMENTS

This section details the preliminary steps in preparation for the first attempt to inject the nanofluid (SiO_2) into a plastic sand-packed slim tube. Prior to nanofluid injection, porosity and permeability measurements were conducted. The calibration of pressure differential transducers is discussed here. The slim tube tested was of 1000 cm in length and 0.4318 cm inner diameter. Measurement of the gas permeability in each stainless steel slim tube apparatus was also attempted, but could not be completed due to blockage within the tube itself.

2.4.1 Transducer Calibration

Four differential pressure transducers (Model DP15) manufactured by Validyne Engineering Corporation were calibrated for use in the slim tube experiment. A standard pressure gauge was used to calibrate transducers with ratings of 12.5, 20, 50, and 125 psi. The signal sent by these transducers is measured in V, and each was calibrated such that atmospheric pressure corresponds to 0 V and its maximum pressure rating corresponds to 10 V. The calibration plots for these transducers are shown in Figures 2.2 – 2.5.

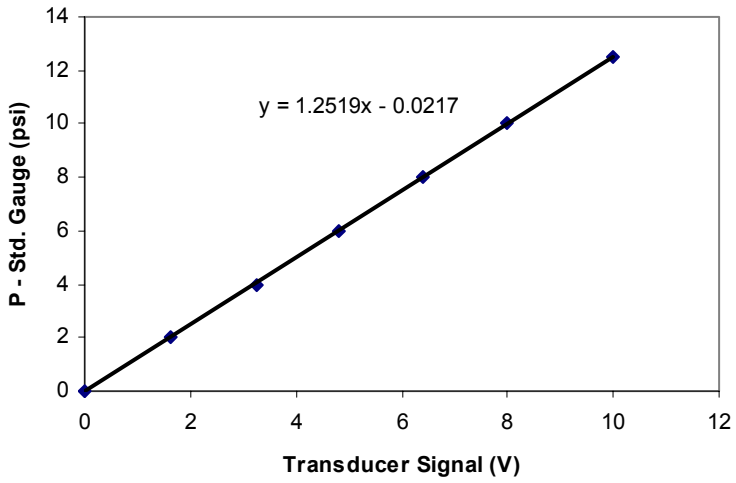

Figure 2.2: Calibration plot of 12.5 psi transducer

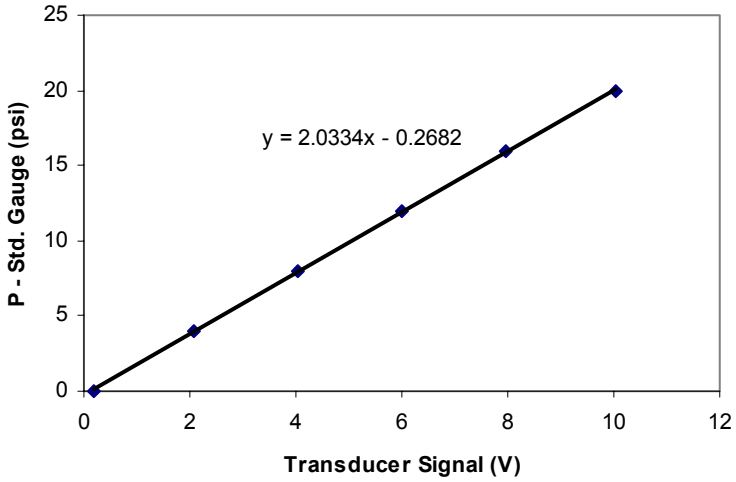

Figure 2.3: Calibration plot of 20 psi transducer

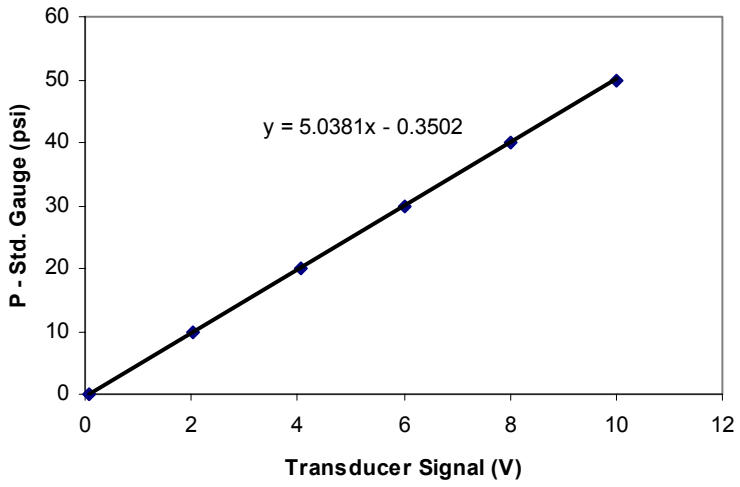

Figure 2.4: Calibration plot of 50 psi transducer

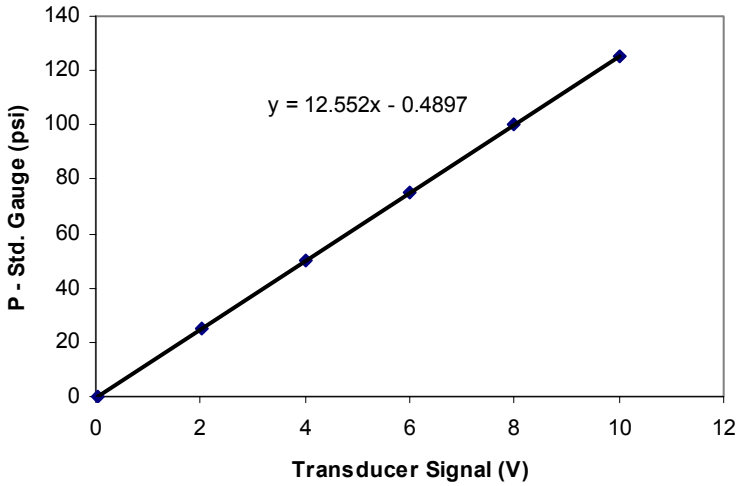

Figure 2.5: Calibration plot of 125 psi transducer

2.4.2 Permeability Measurement in the Stainless Steel Tube

Gas permeability measurements in both stainless steel slim tubes were attempted using the apparatus shown in Figure 2.6. Nitrogen (N_2) gas was directed to flow into the inlet of the coils. The inlet and outlet pressures were measured using differential pressure transducers of 125 and 50 psi ratings, respectively. The flow rates at the outlet were to be measured using a stop-watch and graduated cylinder (the standard method of measuring the flow rate).

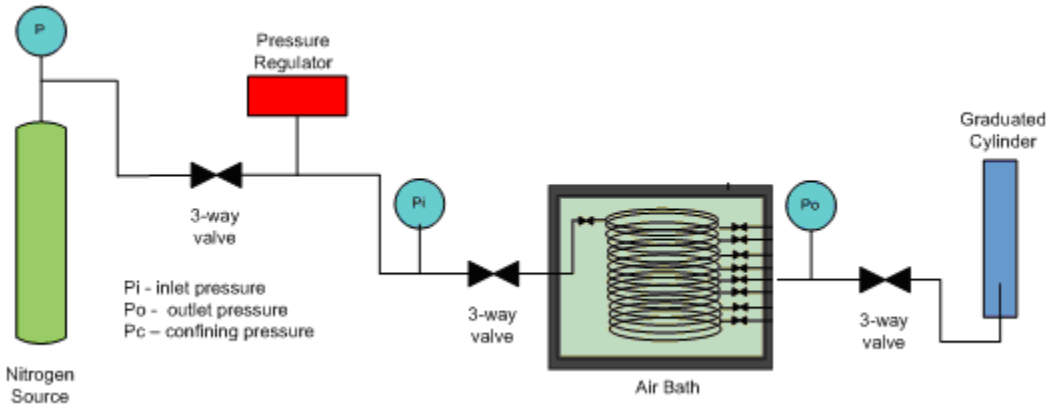

Figure 2.6: Schematic of the apparatus for measuring gas permeability.

In order to best conduct the permeability measurement, it is useful to have reasonable estimates of both the required inlet pressure and residence time corresponding to different gas flow rates. Preliminary calculations were performed using Darcy's law for incompressible flow:

$$k_{gas} = \frac{2\mu p_{out} q_{out} L}{A(p_{in}^2 - p_{out}^2)} \tag{2.1}$$

where μ is the viscosity in cP, q_{out} is outlet volumetric flow rate in cm^3/second, A is the core cross-sectional area in cm^2, L is the core length in cm and p_{in} and p_{out} are inlet and outlet absolute pressures in atmospheres, respectively.

The required inlet pressure corresponding to gas flow rate is shown in Figure 2.7 for three equally likely permeability values.

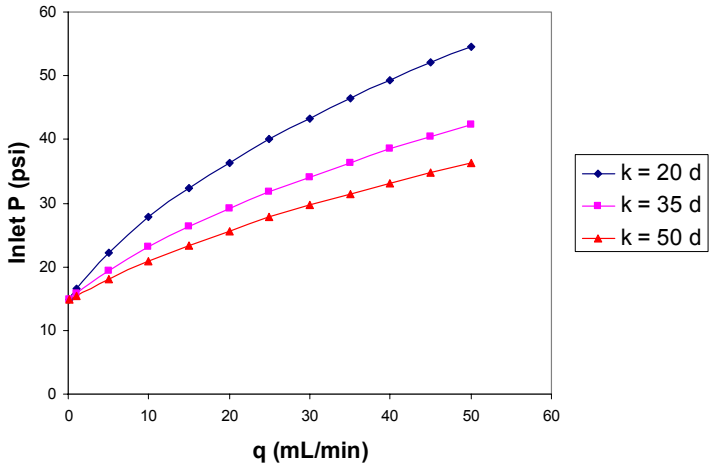

Figure 2.7: Required inlet pressure with varied gas flow rate

The residence time corresponding to gas flow rate is shown in Figure 2.8.

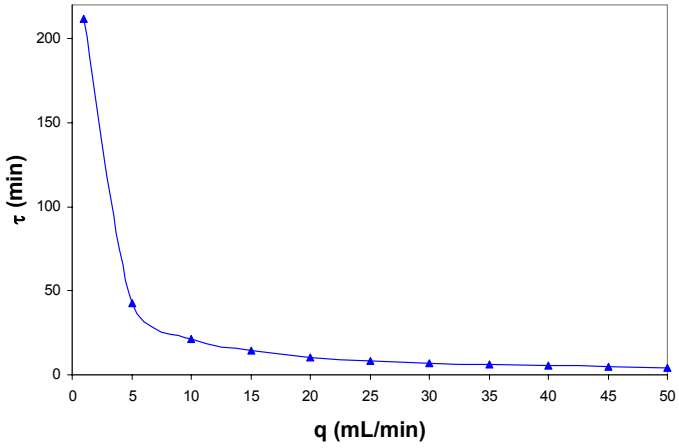

Figure 2.8: Residence time t with varied gas flow rate

The permeability values of the stainless steel slim tubes could not be measured, because gas flow was not achieved at the outlet of either slim tube, even when pressures as high as 600 psi were applied. The effect of reversing the configuration so that the inlet was at the bottom and the outlet at the top was also investigated, with no outlet flow resulting. After checking each valve along the tube for flow, it was determined that only a 10 m section of one tube and a 5 m section of the other were open to flow. Two more stainless steel slim tubes of the same length were then constructed and successfully tested for flow at the outlet. It should be noted that one of these new slim tubes was constructed without valves, as it is possible that the blockage in the first tubes was caused by the welding of the valve ports themselves.

2.4.3 Permeability Measurement in Polypropylene Slim Tube

The gas permeability was measured, and the Klinkenberg effect (gas slippage) was considered to evaluate the equivalent liquid permeability. The liquid permeability of the slim tube was then measured.

The apparatus used in the measurement of gas permeability was identical to the one shown in Figure 2.7 for the stainless steel slim tubes. The gas flowed in this experiment was nitrogen (N_2). The inlet and outlet pressures were measured using differential pressure transducers of 125 and 50 psi ratings, respectively. The flow rate at the outlet was measured using a stop-watch and graduated cylinder (the standard method of measuring the flow rate).

The gas permeability measurement was started by introducing nitrogen at different flow rates and inlet pressures. The average gas permeability was found to be around 50.2 darcy by applying Darcy's law for compressible fluids which is given by Equation 2.1.

The gas permeability as a function of the reciprocal of mean pressure is depicted in Figure 2.9. According to the Klinkenberg effect, extrapolating the straight line to infinite mean pressure (or zero reciprocal of mean pressure) intercepts the permeability axis at a point designated as the equivalent liquid permeability (Amyx, Bass, and Whiting, 1960). In Figure 2.9, the average equivalent liquid permeability is 40.2 darcy.

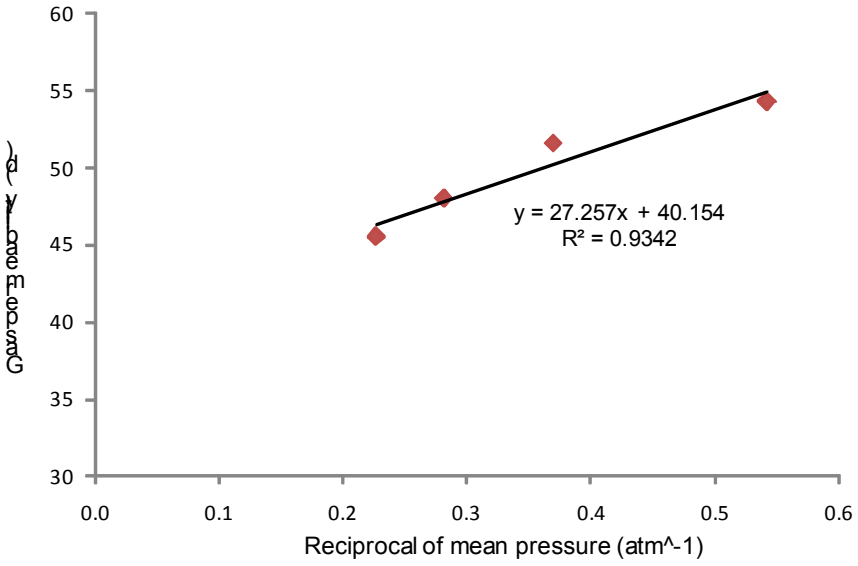

Figure 2.9: Gas permeability versus the reciprocal of mean pressure

The liquid permeability was measured on the same tube. A schematic of the apparatus used in the measurement of liquid permeability is shown in Figure 2.10.

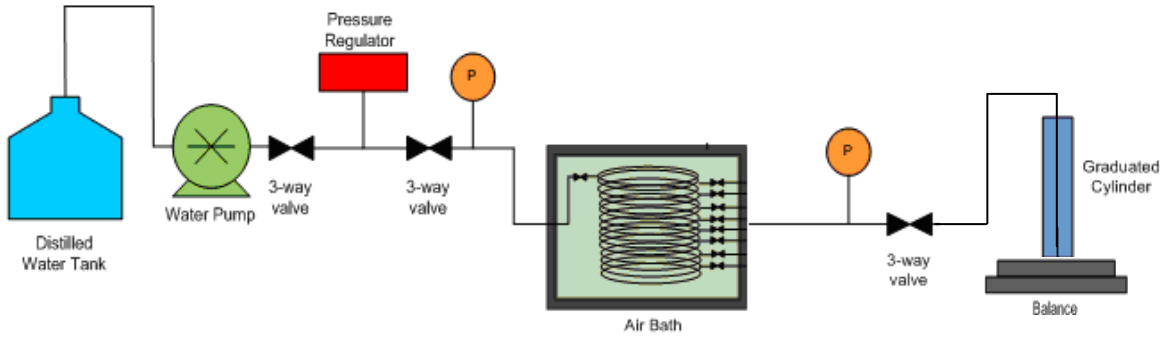

Figure 2.10: Schematic of apparatus for liquid permeability measurement

The sand-packed slim tube and related system were evacuated using a Welch Vacuum Pump for 4 hours at a vacuum pressure of about 25 millitorr to remove moisture. A column of pure water of known weight (W_d) was introduced to saturate the entire sand-packed and inlet tubes. The new water column weight (W_s) was then noted. The sand-packed slim tube turned out to have a porosity of around 35.5 % and a pore volume of 51.9 cm^3. The porosity calculation is as follows:

$$\phi = \frac{V_p}{V_B} * 100 \tag{2.2}$$

$$V_{p1} = W_s - W_d \tag{2.3}$$

$$V_{p2} = \pi r_t^2 l_t \tag{2.4}$$

$$V_p = V_{p1} - V_{p2} \tag{2.5}$$

$$V_B = \pi r^2 l \tag{2.6}$$

where ϕ is the porosity in percentage, V_p and V_B are pore and bulk volumes of sand-packed tube in cm^3, respectively. V_{p1} is the total of the sand-packed tube pore volume plus the inlet tubes dead volume in cm^3. V_{p2} is the dead volume of inlet tubes in cm^3. W_s and W_d are the weight of water column after and before saturation, in g, respectively. r and l are the radius and length of the sand-packed tube in cm, respectively. r_t and l_t are the radius and length of the inlet tubes in cm, respectively.

The same differential pressure transducers were used as previously in the gas permeability measurement. In addition, a water pump was used to inject pure water and the flow rate measured using a stop-watch and a Mettler balance (Model PE 300). The pump calibration curve can be found in the first quarterly report (January-March 2009).

Following the saturation, the liquid permeability was measured by injecting pure water using the water pump. Several flow rates were used to calculate the liquid permeability, ranging from 1 to 3 ml/min at different differential pressures. The average liquid

permeability was found to be around 49.9 darcy. Darcy's law for horizontal flow was utilized to compute the permeability. Darcy's law for horizontal flow is given by:

$$k_{liq} = \frac{q\mu L}{A\Delta p} \tag{2.7}$$

where q is the volumetric flow rate in ml/second, μ is the viscosity in cP, L and A are the length and the cross-sectional area of the slim tube in cm and cm^2, respectively. Δp is the differential pressure across the slim tube in atmospheres.

2.4.4 Nanofluid injection experiment

This section outlines the plan to inject nanoparticles into the long sand-packed slim tubes. The objective of this experiment is to investigate the transport and recovery of nanoparticles through a longer flow path. This is to approach actual field distances such as in interwell tracer testing. For that, 10 m sand-packed slim tube flow apparatus was constructed. A schematic of the apparatus is shown in Figure 2.11. Nanofluid solution will be contained in a pressure vessel downstream of the water pump. The nanofluid will be injected into the slim tube with the aid of nitrogen pressure. The configuration also allows for injection of particle-free water, without interrupting the flow. This experiment will not consider the temperature effect, so will be conducted at room temperature.

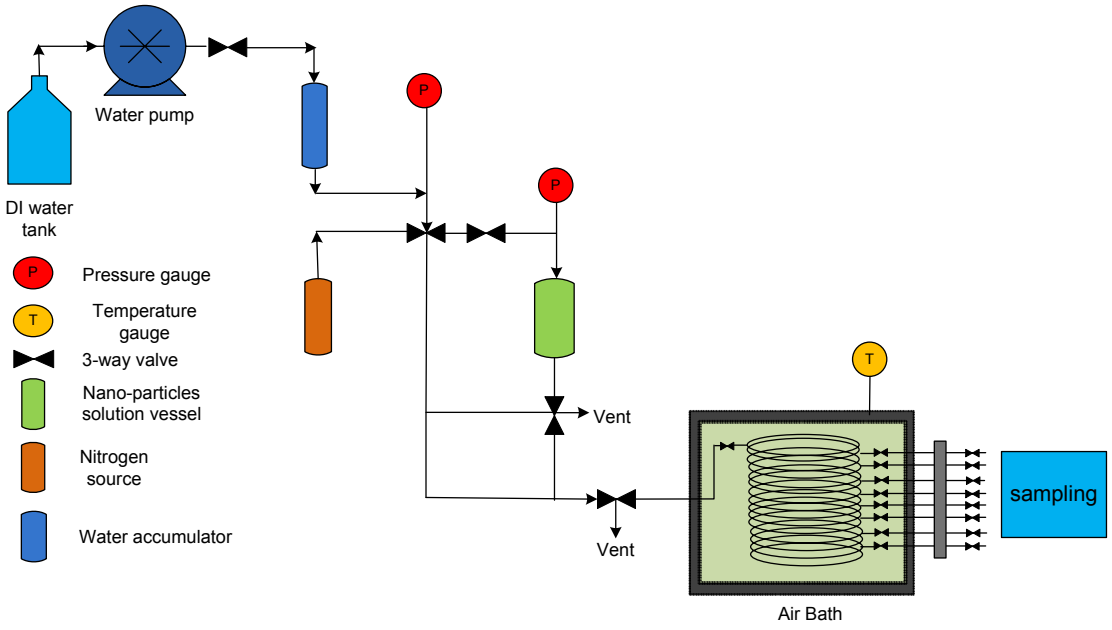

Figure 2.11: Experimental apparatus for nanofluid injection into sand-packed tube.

The SiO_2 nanoparticles prepared for injection had an average particle size of approximately 350 nanometers as shown in Figures 2.12 and 2.13, determined by light scattering and scanning electron microscopy, respectively.

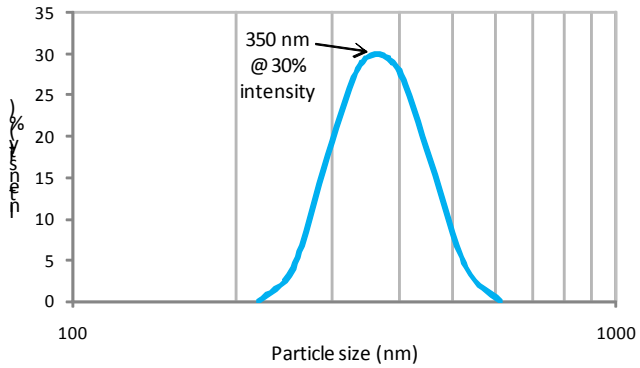

Figure 2.12: Particle size distribution by light intensity percentage of the influent injected.

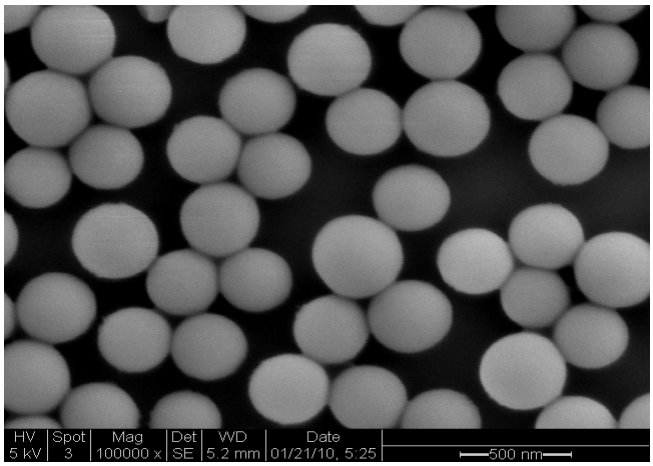

Figure 2.13: Monodisperse SiO_2 nanospheres of the influent with an average size of 350 nm.

Prior to the injection of the nanofluid, the slim tube will be preflushed with pure water to displace any debris (4 pore volumes in this case). It is planned to inject nanofluid of about 20% of the pore volume (i.e. 10 ml) followed by a continuous injection of pure water. The pore volume was determined as outlined in Section 2.4.2. The injected volume calculation is as follows:

$$V_p = V_B \phi \tag{2.8}$$

$$V_d = \pi r_t^2 l_t \tag{2.9}$$

$$V_{inj} = 0.2 * V_p + V_d \tag{2.10}$$

where r_t and l_t are the radius and length of the inlet tube in cm, respectively. V_d and V_{inj} are the dead and total injected volumes in cm^3, respectively. The rest of parameters have their usual definition.

Subsequent to the injection of the nanofluid (pore and dead volumes), a continuous flow of pure water will be introduced. Specifically, eight (8) pore volumes of pure water will be injected while the effluent samples are constantly collected. The injection will be at the rate of two ml/minute to facilitate the sampling operation. Frequent sampling during the first two pore volumes is planned. Not all these samples will be analyzed but rather a careful selection of some will be conducted to optimize the analysis time.

The slim tube will be then backflushed with few pore volumes. This will be an attempt to determine whether there are any trapped nanoparticles, especially that the inlet.

2.5 FUTURE WORK

The next stage will be to inject the nanoparticles into the 10 m sand-packed slim tube. The effluent samples will be characterized using dynamic light scattering as well as scanning electron microscopy.

An injection of hematite nanorice is also planned. The objective of this experiment is to investigate the feasibility of flowing nonspherical nanoparticles through porous media. The testing of this idea was initiated earlier by the injection of sliver nanowires. The details of this experiment can be found in last quarter report (July-September 2009). The silver nanowires were found trapped at the inlet of the sandstone core. Note that they had a longitudinal dimension in the range of 5-10 μm. It has been concluded that their geometry may have imposed constraint on their transportation through the core. To test this hypothesis, a trial injection of shorter wire-like nanoparticles or nanorice (less than 1 micron length) will be conducted. Both the Berea sandstone and the sand-packed slim tube will be used in this test.

3. FRACTURE CHARACTERIZATION USING RESISTIVITY

This research project is being conducted by Research Assistant Lilja Magnusdottir, Senior Research Engineer Kewen Li and Professor Roland Horne. The objective of this project is to investigate ways to use resistivity to infer fracture properties in geothermal reservoirs.

3.1 SUMMARY

The aim of this part of the project is to use resistivity measurements and modeling to characterize fracture properties in geothermal fields. The resistivity distribution in the field can be estimated by measuring potential differences between various points and the resistivity data can be used to infer fracture properties due to the large contrast in resistivity between water and rock.

This report describes the first phase of the project where a two-dimensional model was made to calculate a potential field due to point sources of excitation. The model takes into account heterogeneity by solving the potential field for inhomogeneous resistivity. Fractures can be modeled as areas with resistivity different from the rock, to investigate the changes in the potential field around them.

Future work will involve using the model to characterize fracture patterns in two dimensions from potential distribution. Ways to enhance the contrast between fracture and rock resistivity will also be explored to ease the fracture characterization. Different resistivity measurements and modeling techniques will be explored as well.

3.2 INTRODUCTION

The designing of optimal production wells in geothermal reservoirs requires knowledge of the resource's connectivity and heat intensity for energy extraction. Drilling and construction of wells are expensive and the energy content from a well depends highly on the fractures it intersects. Fracture characterization is therefore important to increase the reliability of geothermal wells and thereby the overall productivity of geothermal power plants.

In this project, the goal is to find ways to use Electrical Resistivity Tomography (ERT) to characterize fractures in geothermal reservoirs. ERT is a technique for imaging the resistivity of a subsurface from electrical measurements. Typically, electrical current is injected into the subsurface through conducting electrodes and the resulting electrical potentials are measured. Due to the large contrast in resistivity between water and rock, the resistivity measurements could be efficiently used to indicate fracture locations.

Resistivity measurements have been widely used in the medical industry to image the internal conductivity of the human body, for example to monitor epilepsy, strokes and lung functions as discussed by Holder (2005). In Iceland, electrical resistivity tomography methods have been used to map geothermal reservoirs. Arnarson (2001) describes how different resistivity measurements have been efficiently used there to locate high temperature fields by using electrodes located on the ground's surface. Stacey et al. (2006) investigated the feasibility of using resistivity to measure geothermal core saturation. A direct current pulse was applied through electrodes attached in rings around a sandstone

core and it resulted in data that could be used to infer the resistivity distribution and thereby the saturation distribution in the core. It was also concluded by Wang (2000) that resistivity data has high resolution power in depth direction and is capable of sensing the areal heterogeneity.

In the approach considered in this project, electrodes are placed inside geothermal wells and the resistivity anomalies between them studied to locate fractures and infer their properties by resistivity modeling. Due to the lack of measurement points, i.e. limited number of test wells, we will endeavor to find ways to ease the process of characterizing fractures from limited resistivity data. To enhance the contrast in resistivity between the rock and fracture zones, the possibility of using conductive fluid will be explored. Furthermore, the influences of temperatures and fluid stream on resistivity measurements will be studied. The effects of mineralization in the fractures will also be examined, since fractures containing a lot of minerals can be more difficult to distinguish from the surrounding rocks. The first part of the project is to make a resistivity model that calculates a potential field due to point sources of excitation, as this report discusses.

3.3 RESISTIVITY MODELING

One of the main problems in resistivity modeling is to solve the Poisson's equation that describes the potential field and to efficiently complete the inversion iteration. That governing equation can be derived from some basic electrical relationships as described by Dey and Morrison (1979). Ohm's Law defines the relationship between current density, J, conductivity of the medium, σ, and the electric field, E, as

$$J = \sigma E \tag{3.1}$$

The stationary electric fields are conservative, so the electric field at a point is equal to the negative gradient of the electric potential there, i.e.

$$E = -\nabla \phi \tag{3.2}$$

where ϕ is the scalar field representing the electric potential at the given point. Hence,

$$J = -\sigma \nabla \phi \tag{3.3}$$

Current density is the movement of charge density, so according to the continuity equation, the divergence of the current density is equal to the rate of change of charge density,

$$\nabla J = \frac{\partial Q(x,y,z)}{\partial t} = q(x,y,z) \tag{3.4}$$

where q is the current density in amp m^{-3}. Combining equations (3.3) and (3.4) gives the following Poisson's equation which describes the potential distribution due to a point source of excitation,

$$\nabla\left[\sigma \nabla \phi\right] = -q(x,y,z) \tag{3.5}$$

The conductivity σ is in mhos m^{-1} and the electric potential is in volts. This partial differential equation can then be solved numerically for the resistivity problem.

3.3.1 Finite Difference Equations in Two Dimensions

Finite difference method was used to approximate the solution to the partial differential equation (3.5) using a point-discretization of the subsurface (Mufti, 1976). The

computational domain was discretized into $Nx \times Ny$ blocks and the distance between two adjacent points on each block is *h*, as shown in Figure 3.1.

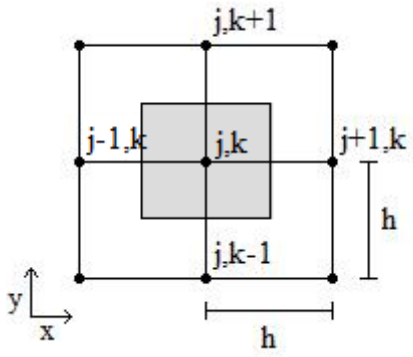

Figure 3.1: Computational domain, discretizied into blocks.

Taylor series expansion is used to approximate the derivatives of equation (3.5) about a point (*j,k*) on the grid,

$$\left.\frac{\partial}{\partial x}\left(\sigma\frac{\partial\phi}{\partial x}\right)\right|_{(j,k)} \approx \frac{\left[\begin{array}{l}\phi(j+1,k)\sigma\left(j+\frac{1}{2},k\right)+\phi(j-1,k)\sigma\left(j-\frac{1}{2},k\right)\\ -\left[\sigma\left(j+\frac{1}{2},k\right)\sigma\left(j-\frac{1}{2},k\right)\right]\phi(j,k)\end{array}\right]}{h^2} \tag{3.6}$$

$$\left.\frac{\partial}{\partial y}\left(\sigma\frac{\partial\phi}{\partial y}\right)\right|_{(j,k)} \approx \frac{\left[\begin{array}{l}\phi(j,k+1)\sigma\left(j,k+\frac{1}{2}\right)+\phi(j,k-1)\sigma\left(j,k-\frac{1}{2}\right)\\ -\left[\sigma\left(j,k+\frac{1}{2}\right)\sigma\left(j,k-\frac{1}{2}\right)\right]\phi(j,k)\end{array}\right]}{h^2} \tag{3.7}$$

The point (*j,k*) represents the shaded area in Figure 3.1 (area = h^2) so the current density due to a electrode at that point is given by,

$$q(j,k) = I / h^2 \tag{3.8}$$

where *I* [amp] is the current injected at point (j,k) Combining Equations (3.5)-(3.8) and solving for the electric potential ϕ at point (j,k) gives,

$$\phi(j,k) = \frac{\left[I + \phi(j+1,k)c_1 + \phi(j-1,k)c_2 + \phi(j,k+1)c_3 + \phi(j,k-1)c_4\right]}{c_1 + c_2 + c_3 + c_4} \tag{3.9}$$

The parameters c_i represents the conductivity averaged between two adjacent blocks, i.e.

$$c_1 = \frac{2}{\rho(j,k) + \rho(j+1,k)} \tag{3.10}$$

$$c_2 = \frac{2}{\rho(j,k) + \rho(j-1,k)} \tag{3.11}$$

$$c_3 = \frac{2}{\rho(j,k) + \rho(j,k+1)} \tag{3.12}$$

$$c_4 = \frac{2}{\rho(j,k) + \rho(j,k-1)} \tag{3.13}$$

where ρ*(j,k)* is the resistivity [ohm-m] of the node at grid coordinates *j,k*.

3.3.2 Iteration method

In order to numerically solve Equation (3.9) and get the results for electrical potential ϕ at each point on the grid, iteration method called Successive Over-Relaxation is used (Spencer and Ware, 2009). At first a guess is made for $\phi(j,k)$ across the whole grid, for example $\phi(j,k)$= for all *j,k*. That guess is then used to calculate the right hand side of Equation (3.9) for each point and the new set of values for $\phi(j,k)$ is calculated using the following iteration scheme,

$$\phi_{n+1} = \omega Rhs + (1-\omega)\phi_n \tag{3.14}$$

The multiplier ω is used to shift the eigenvalues so the iteration converges better than simple relaxation. The number ω is between 1 and 2, and when the computing region is rectangular the following equation can be used to get a reasonable good value for ω,

$$\omega = \frac{2}{1+\sqrt{1-R^2}} \tag{3.15}$$

where

$$R = \frac{\left(\cos\left(\frac{\pi}{Nx}\right) + \cos\left(\frac{\pi}{Ny}\right)\right)}{2} \tag{3.16}$$

The natural Neumann boundary condition is used on the outer boundaries in this project, i.e. $\frac{\partial\phi}{\partial n} = 0$.

3.4 RESULTS

The resistivity model is first tested for a 160×160 m field with homogeneous resistivity as 1 Ωm. A current is set equal to 1 A at a point in the upper left corner, and as -1 A at the lower right corner. The potential distribution can be seen in Figure 3.2.

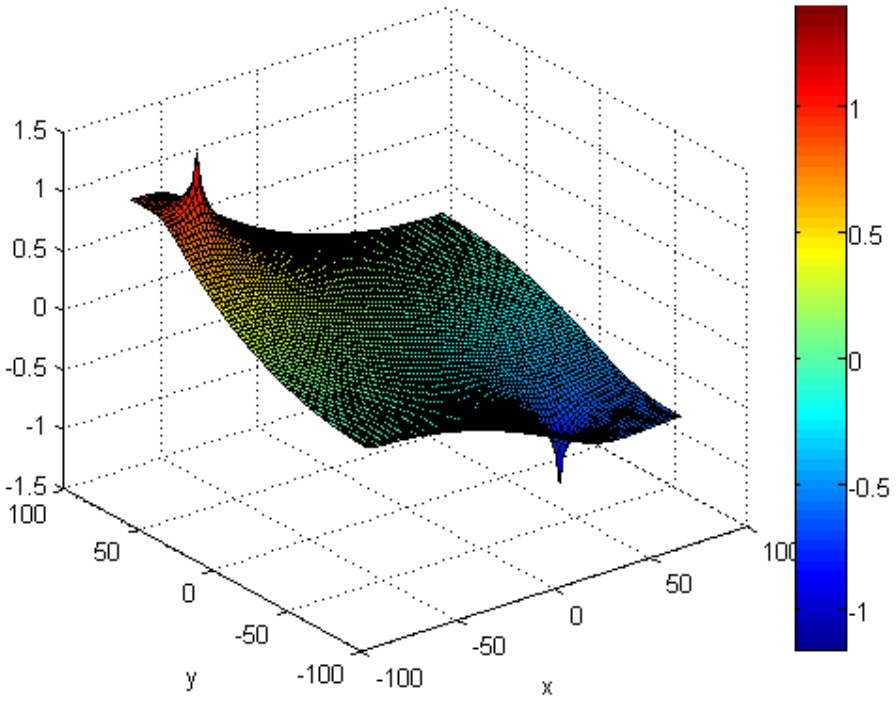

Figure 3.2: Potential distribution [V] for a homogeneous resistivity field.

The program gives similar results as the Partial Differential Equation (PDE) ToolboxTM in Matlab gives for similar field, as can be seen by comparing Figures 3.3 and 3.4.

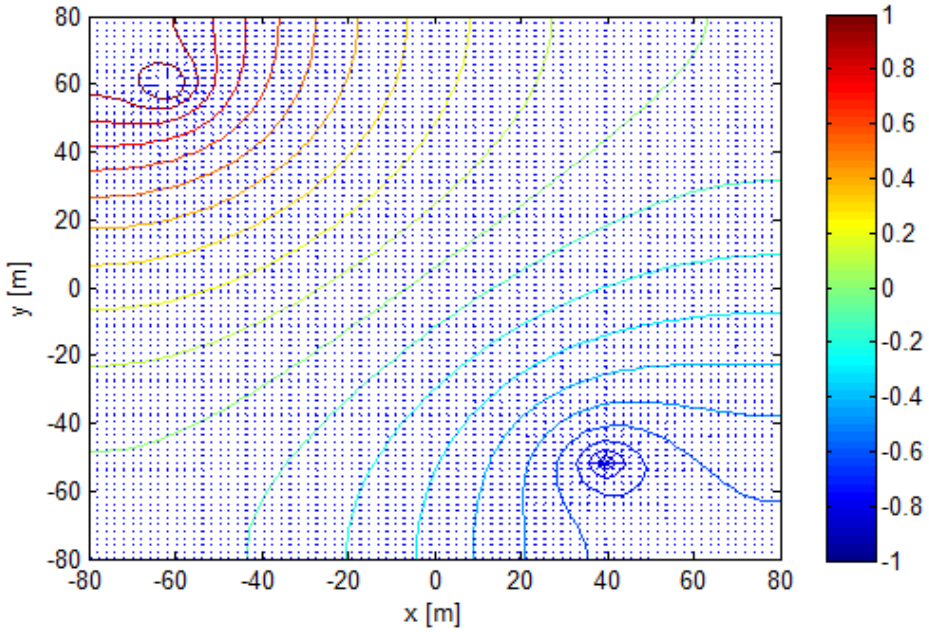

Figure 3.3: Potential distribution [V] for a homogeneous resistivity field, calculated using the model.

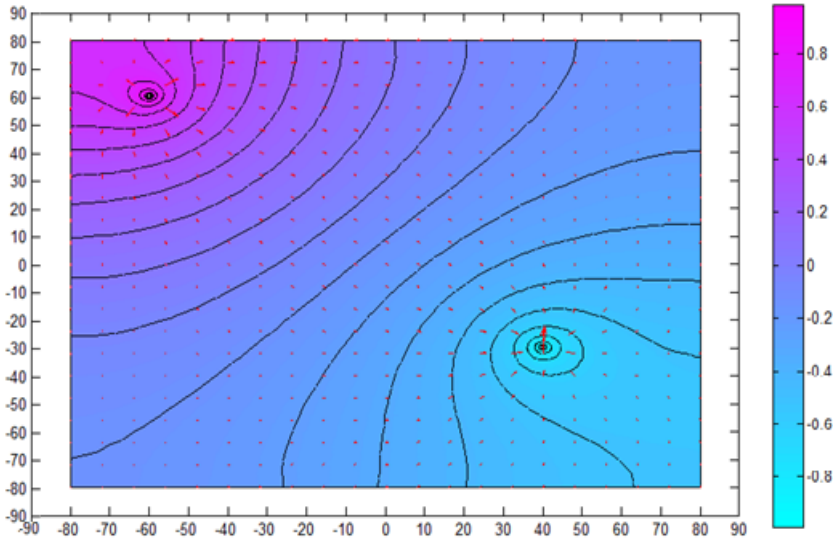

Figure 3.4: Potential distribution for a homogeneous resistivity field, calculated using PDE Toolbox in Matlab.

The Partial Differential Equation Toolbox™ in Matlab contains tools to preprocess, solve and postprocess partial differential equations in two dimensions (MathWorks, 2003). However, it does not solve a potential field for inhomogeneous resistivity. In order to use the potential differences to distinguish between the rock and fractures, the model calculating the potential field must be able to take into account heterogeneity, as the model in this project does. Figure 3.5 shows the potential field where the points on a line between the points where the current is injected have resistivity 10,000 Ωm, while the rest of the field has resistivity 1 Ωm. The field is 160×160 m as before, and a current equal to 1 A is injected in the upper left corner and -1 A in the lower right corner.

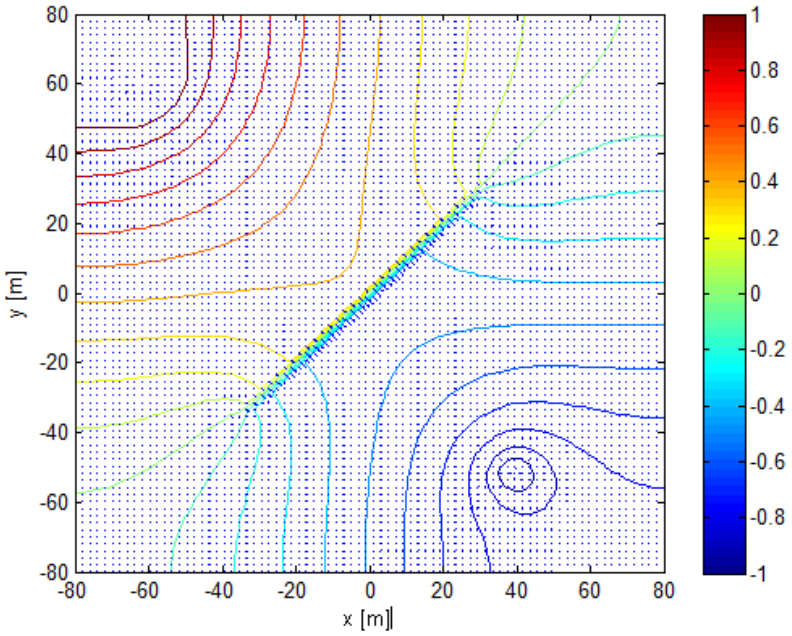

Figure 3.5: Potential distribution for an inhomogeneous resistivity field.

The potential field is higher than for a field with homogeneous resistivity (see Figure 3.3) and the electric field is higher at the high resistivity zone. Different patterns of high resistivity zones can be modeled to investigate whether the change in the electrical potential can infer the fracture pattern. Figures 3.6-3.7 show potential fields for different patterns.

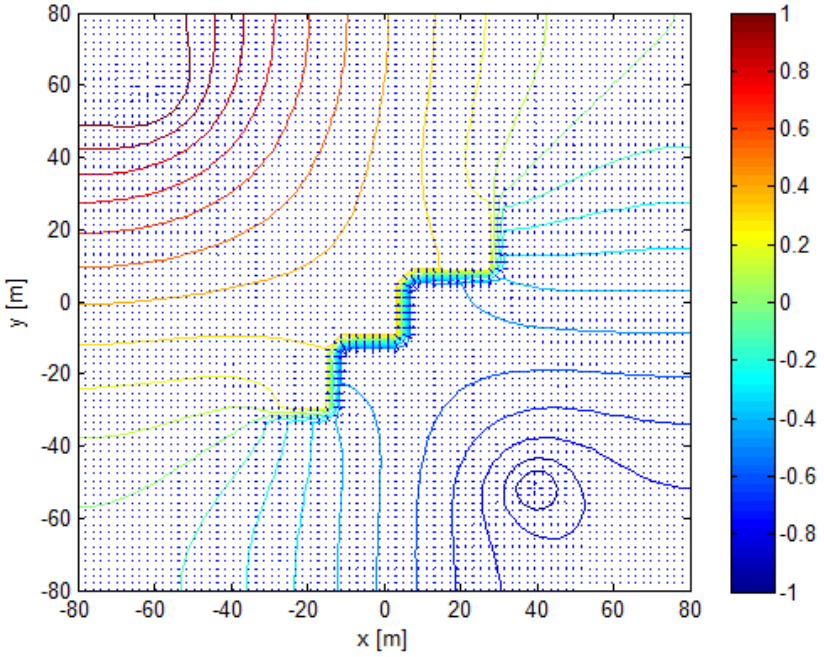

Figure 3.6: Potential distribution for fracture pattern 1.

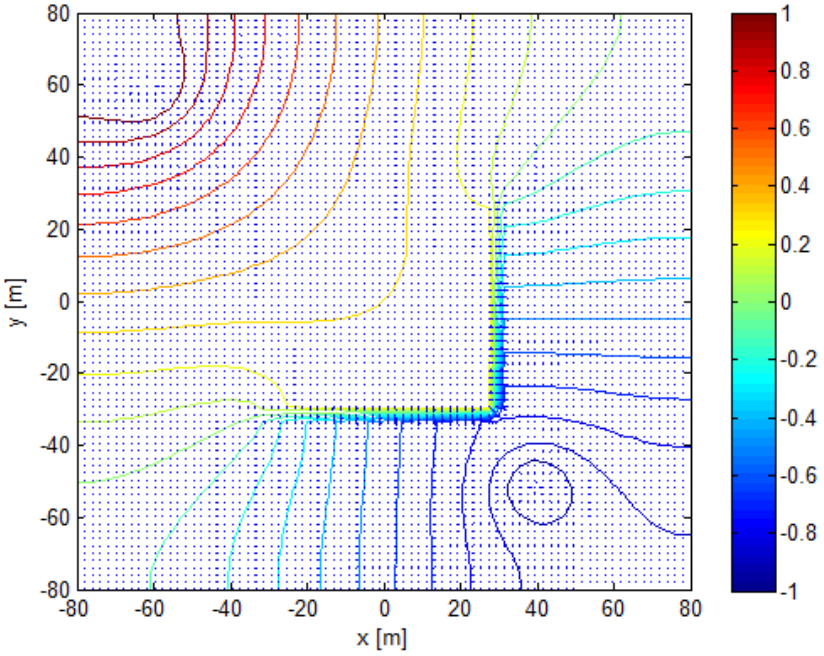

Figure 3.7: Potential distribution for fracture pattern 2.

The electric potentials are different in Figure 3.6 and Figure 3.7 but more information about the fractures can be obtained by injecting currents in the upper right corner and lower left corner, as shown in Figures 3.8 and 3.9.

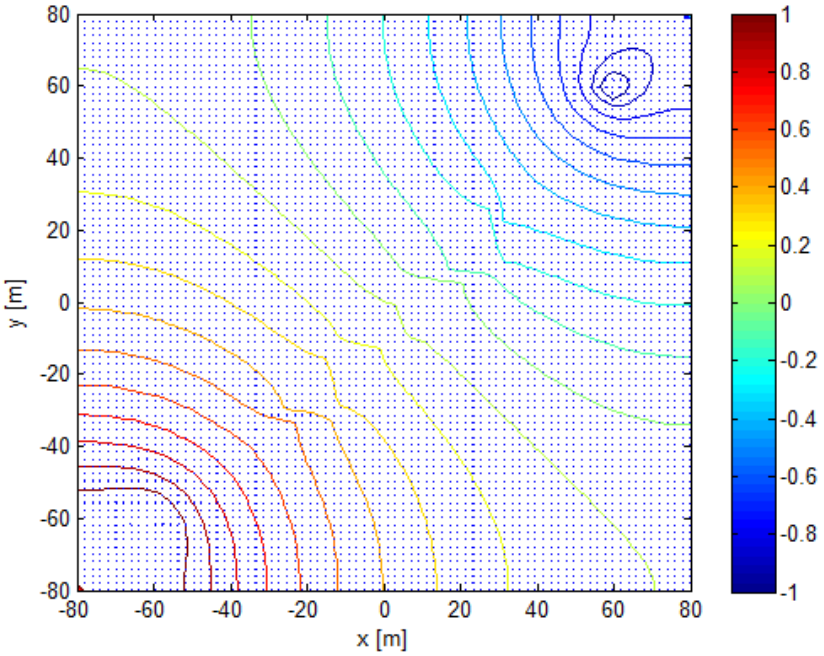

Figure 3.8: Potential distribution for fracture pattern 1 when current is injected in upper right and lower left corners.

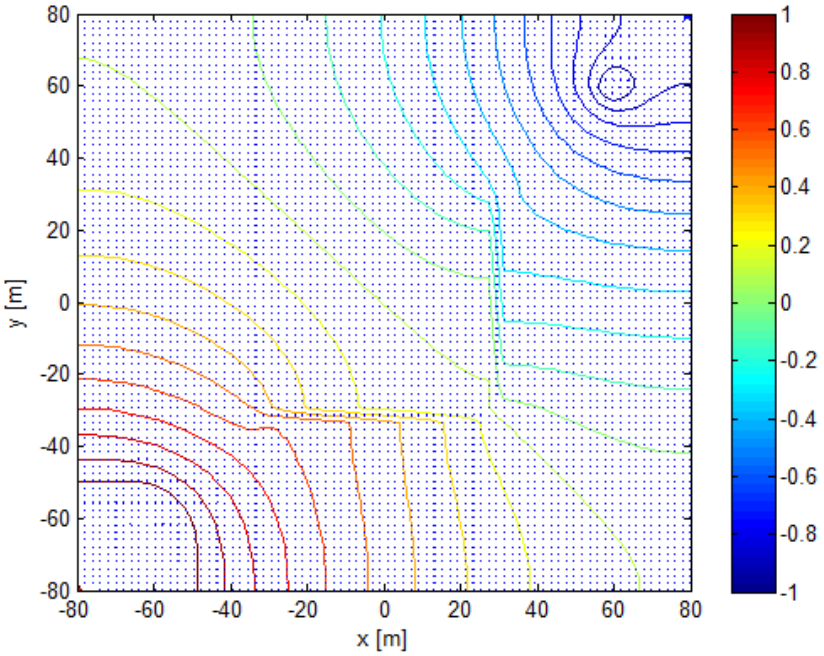

Figure 3.9: Potential distribution for fracture pattern 2 when current is injected in upper right and lower left corners.

Fracture pattern 1 cannot be as easily detected in Figure 3.8 as fracture pattern 2 in Figure 3.9, since fracture pattern 1 lies almost in the same direction as the current going from one point to the other. The figures show how the electrical potential distribution varies with high resistivity patterns and how different potential fields are established for different locations of the current excitation. The difference due to varying resistivity can hopefully be used to characterize the patterns to infer fracture properties.

3.5 FUTURE WORK

One of the next steps is to use the program to look at potential fields for more realistic fracture patterns and to investigate ways to characterize the patterns using the potential differences all around the fractures. If the fractures can be characterized that way, the more complex case will be examined where the potential difference is only measured between a few points, since there would only be a few test wells in a geothermal reservoir where the potential difference could be measured. Another near future step is to explore the possibility of using conductive fluid to enhance the difference between fracture and rock resistivity, making it easier to distinguish between the two.

Other future goals are to study the influences of temperatures on water resistivity as well as the potential changes due to fluid stream in the fractures. Also, the effects of mineralization will be examined because it can be difficult to distinguish between rock and fractures containing a lot of minerals.

4. REFERENCES

Amyx, J. W., Bass, D. M. Jr., and Whiting, R. L. (1960), *Petroleum Reservoir Engineering, Physical Properties.* McGraw-Hill Book Co.

Alaskar, Mohammed N., Horne, R.N.. and Li, Kewen (2009), "Fracture Characterization of Enhanced Geothermal Systems Using Nanoparticles," DOE quarterly report (2009 January to March), Contract DE-FG36-08GO18192, 17-29.

Alaskar, Mohammed N., Horne, R.N.. and Li, Kewen (2009), "Fracture Characterization of Enhanced Geothermal Systems Using Nanoparticles," DOE quarterly report (2009 July to September 2009), Contract DE-FG36-08GO18192, 17-29.

Arnason, K.: Viðnámsmælingar í Jarðhitarannsóknum á Íslandi, Orkustofnun, Orkuþing (2001).

Bear, J., Dynamics of fluids in porous media, *Dover*, (1972), pp. 1-764.

Bodvarsson, G., and Pruess, K., Thermal effects of reinjection in geothermal reservoirs with major vertical fractures, *Journal of Petroleum Technology*, **36**, (1984), 1567–1578.

Cao, H., Development of techniques for general purpose simulators, Ph.D. Thesis, Stanford University. Stanford, CA, (2002).

Dey, A. and Morrison, H.F.: Resistivity Modelling for Arbitararily Shaped Two-Dimensional Structures, Geophysical Prospecting 27, I06-I36, University of California, Berkeley, CA (1979).

Gong, B., Effective models of fractured systems, Ph.D Thesis, Stanford University, Stanford, CA, (2007).

Holder, D.S.: Electrical Impedance Tomography: Methods, History and Applications, IOP, UK (2004).

Horne, R., and Rodriguez, F., Dispersion in tracer flow in fractured geothermal systems, *Proceedings of Seventh Workshop on Geothermal Reservoir Engineering*, Stanford University, Stanford, CA, (1983), 103-107.

Horne, R., and Szucs, P., Inferring Well-to-Well Connectivity Using Nonparametric Regression on Well Histories, *Proceedings of Thirty-Second Workshop on Geothermal Reservoir Engineering*, Stanford University, Stanford, CA, (2007).

Juliusson E. and Horne, R.N., Fracture characterization using production and injection data, DOE quarterly report (2009 January to March), Contract DE-FG36-08GO18192, Stanford Geothermal Program, Stanford University, California, (2009a), 1-17.

Juliusson E. and Horne, R.N.: Fracture characterization using production and injection data, DOE quarterly report (2009 July to September), Contract DE-FG36-08GO18192, Stanford Geothermal Program, Stanford University, California, (2009b), 1-24.

Karimi-Fard, M., Durlofsky, L. and Aziz, K., An Efficient Discrete Fracture Model Applicable for General Purpose Reservoir Simulators, *Proceedings of SPE Reservoir Simulation Symposium*, (2003), 1-11.

Lange, A., Bousian, J. and B. Bourbiaux., Tracer-Test Simulation on Discrete Fracture Network Models for the Characterization of Fractured Reservoirs, *SPE Europec/EAGE Annual Conference,* (2005), 1-10.

Lovekin, J. and Horne, R., Optimization of injection scheduling in geothermal fields, Conference, *Proceedings of the Geothermal Program Review VII*, (1989), 45-52.

MathWorks: Partial Differential Equation Toolbox 1, The MathWorks™, Inc. (2003).

Mufti, I.R.: Finite-Difference Resistivity Modeling for Arbitrarily Shaped Two-Dimensional Structures, *Geophysics*, **41**, (1976), 62-78.

Shewchuk, J., Triangle: Engineering a 2D quality mesh generator and Delaunay triangulator, *Lecture Notes in Computer Science*, **1148**, (1996), 203–222.

Spencer, R.L. and Ware, M.: Computational Physics 430, Partial Differential Equations, Department of Physics and Astronomy, Brigham Young University (2009).

Stacey, R.W., Li, K. and Horne, R.N.: Electrical Impedance Tomography (EIT) Method for Saturation Determination, *Proceedings*, 31st Workshop on Geothermal Reservoir Engineering, Stanford University, Stanford, CA (2006).

Sullera, M., and Horne, R., Inferring injection returns from chloride monitoring data, *Geothermics*, **30**, (2001), 591–616.

Urbino, E. G., and Horne, R., Optimizing reinjection strategy at Palinpinon, Philippines, based on chloride data, *Proceedings of Sixteenth Workshop on Geothermal Reservoir Engineering*, Stanford University, Stanford, CA, (1991).

Voskov, D., Description of the Thermal GPRS, Technical Report, Department of Energy Resources Engineering, Stanford University, (2006).

Wang, P. and Horne, R.N.: Integrating Resistivity Data with Production Data for Improved Reservoir Modelling, SPE 59425, SPE Asia Pacific Conference, Yokohama, Japan (2000).

Wu, Y., Numerical simulation of non-isothermal multiphase tracer transport in heterogeneous fractured porous media, *Advances in Water Resources*, **23**, (2000), 699-723.

Wu, Y. and Forsyth, P.A., Efficient Schemes for Reducing Numerical Dispersion in Modeling Multiphase Transport through Heterogeneous Geological Media, *Vadose Zone Journal*, **7**, (2008), 340-349.